HHS Public Access

Author manuscript

Cell Rep. Author manuscript; available in PMC 2026 May 20.

Published in final edited form as:

Cell Rep. 2026 March 24; 45(3): 117073. doi:10.1016/j.celrep.2026.117073.

Single-cell epigenomics uncovers heterochromatin instability and transcription factor dysfunction during mouse brain aging

Maria Luisa Amaral[1,2], **Sainath Mamde**[1], **Michael Miller**[3], **Xiaomeng Hou**[3], **Jessica Arzavala**[4], **Julia Osteen**[4], **Nicholas D. Johnson**[4], **Elizabeth Walker Smoot**[3], **Qian Yang**[3], **Emily Eisner**[3], **Qiurui Zeng**[5,6], **Cindy Tatiana Báez-Becerra**[4], **Jacqueline Olness**[3], **Joseph Colin Kern**[3], **Jonathan Rink**[4], **Ariana Barcoma**[4], **Silvia Cho**[4], **Stella Cao**[4], **Nora Emerson**[4], **Jasper Lee**[4], **Jackson Willier**[4], **Timothy Loe**[1], **Henry Jiao**[3], **Songpeng Zu**[1], **Quan Zhu**[3], **Sebastian Preissl**[3,7,8,9,10], **Allen Wang**[3], **Joseph R. Ecker**[5,11], **Maria Margarita Behrens**[4,*], **Bing Ren**[1,12,13,14,*]

[1]Department of Cellular and Molecular Medicine, School of Medicine, University of California, San Diego, La Jolla, CA 92093, USA

[2]Bioinformatics and Systems Biology Program, University of California, San Diego, La Jolla, CA 92093, USA

[3]Center for Epigenomics, School of Medicine, University of California, San Diego, La Jolla, CA 92093, USA

[4]Computational Neurobiology Laboratory, The Salk Institute for Biological Studies, La Jolla, CA 92037, USA

[5]Genomic Analysis Laboratory, The Salk Institute for Biological Studies, La Jolla, CA 92037, USA

[6]Division of Biological Sciences, University of California, San Diego, La Jolla, CA 92093, USA

[7]Institute of Experimental and Clinical Pharmacology and Toxicology, Faculty of Medicine, University of Freiburg, Freiburg, Germany

[8]CIBSS – Centre for Integrative Biological Signaling Studies, University of Freiburg, Freiburg, Germany

*Correspondence: mbehrens@salk.edu (M.M.B.), bren@nygenome.org (B.R.).

AUTHOR CONTRIBUTIONS

B.R., J.R.E., M.M.B., and M.L.A. conceived and designed the study. M.L.A. performed the analysis and drafted the manuscript. J. Osteen, A.B., J.R., N.D.J., and S. Cao contributed to tissue dissection and nuclei production. M.M., Q.Y., E.E., and E.W.S. generated the 10× Multiome data. X.H. generated the snATAC-seq data under the supervision of S.P. A.W. oversaw data generation for scATAC and 10× Multiome data. C.T.B.-B., J.A., S. Cho, N.E., and J.L. generated the MERFISH data. J. Olness and J.C.K. preprocessed the MERFISH data under the supervision of Q. Zhu. Q. Zeng analyzed the shared snm3c-seq data and calculated the ABC scores. S.M. performed the RNA doublet removal. S.Z. provided the datasets for label transfer. M.L.A., S.M., and T.L. managed the public data release. J.R.E., M.M.B., M.L.A., and B.R. coordinated the research and edited the manuscript. B.R. supervised the data collection and analysis.

DECLARATION OF INTERESTS

J.R.E. is a member of the scientific advisory board for Zymo Research and Ionis. B.R. is a co-founder and consultant of Arima Genomics Inc. and co-founder of Epigenome Technologies.

DECLARATION OF GENERATIVE AI AND AI-ASSISTED TECHNOLOGIES IN THE WRITING PROCESS

During the preparation of this work, the authors used ChatGPT5.2 in order to shorten the main text to fit within the word limit. After using this tool/service, the authors reviewed and edited the content as needed and take full responsibility for the content of the publication.

[9]Department of Pharmacology and Toxicology, Institute of Pharmaceutical Sciences, University of Graz, 8010 Graz, Austria

[10]Field of Excellence BioHealth, University of Graz, Graz, Austria

[11]Howard Hughes Medical Institute, The Salk Institute for Biological Studies, La Jolla, CA 92037, USA

[12]New York Genome Center, New York, NY 10013, USA

[13]Departments of Genetics and Development, Biochemistry and Molecular Biophysics, and Systems Biology, Vagelos College of Physicians and Surgeons, Columbia University Irving Medical Center, New York, NY 10032, USA

[14]Lead contact

SUMMARY

The mechanisms regulating transcriptional changes during brain aging remain poorly understood. Here, we use single-cell epigenomics to profile chromatin accessibility and gene expression across eight mouse brain regions at 2, 9, and 18 months of age. In addition to a marked decline in progenitor populations involved in neurogenesis and myelination, we observe widespread and concordant age-associated changes in transcription and chromatin accessibility across both neuronal and glial cell types. These alterations are accompanied by dysregulation of master transcription factors and a shift toward stress-response programs driven by activator protein 1 (AP-1), indicating progressive drift in cellular identity with aging. We further identify region- and cell-type-specific heterochromatin loss, characterized by increased accessibility at H3K9me3-marked domains, activation of transposable elements, and upregulation of long noncoding RNAs, particularly in glutamatergic neurons. Together, these findings reveal age-related disruption of heterochromatin maintenance and transcriptional regulation, highlighting vulnerable brain regions, cell types, and molecular pathways in brain aging.

In brief

Amaral et al. present a single-cell atlas of brain aging, revealing coordinated chromatin and gene expression changes across multiple regions from young to old mice. Their analyses show that aging involves loss of progenitor cells, dysregulation of master transcription factors, and destabilization of heterochromatin, driving a gradual erosion of cellular identity.

Graphical Abstract

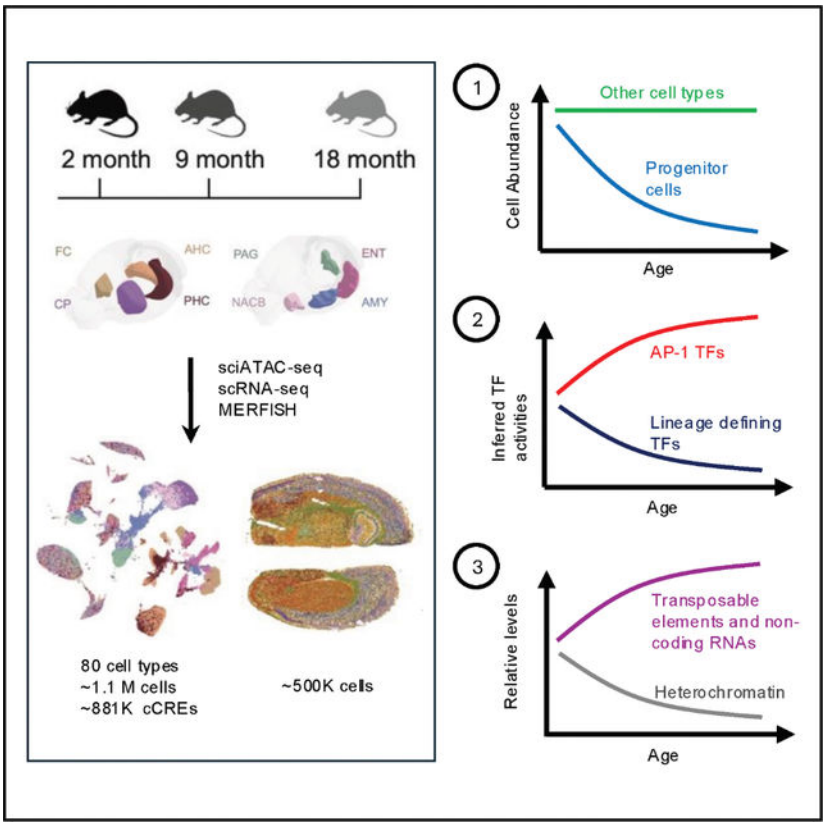

INTRODUCTION

Aging is accompanied by widespread cellular and molecular changes in the brain, which contribute to cognitive decline, reduced neural plasticity, and increased vulnerability to neurodegenerative diseases.[1] While gene expression alterations have been extensively analyzed at single-cell resolution,[2,3] the transcriptional regulatory mechanisms that shape these changes remain largely unresolved. Epigenetic processes, manifested as chromatin accessibility, DNA methylation, histone modifications, and 3D chromatin organization, play a crucial role in defining cellular identity and responsiveness to environmental cues,[4] yet how epigenomic landscapes shift with age across different brain regions and cell types is not well understood.

Recent studies have uncovered conserved hallmarks of aging across tissues, including stem cell exhaustion, mitochondrial dysfunction, genomic instability, and inflammation.[5] Epigenetic alterations have emerged as key contributors to aging,[6] with changes in chromatin accessibility, DNA methylation, and histone modifications linked to a progressive loss of transcriptional fidelity and cellular identity.[7]

Notably, epigenetic aging is also a reversible process, as ectopic expression of pluripotency factors,[8] activation of SIRT6 histone deacetylase,[9,10] and modulation of other histone-modifying enzymes[11,12] have been shown to mitigate certain aging phenotypes. However, prior studies on brain aging largely rely on bulk tissue analyses, which obscure cell-intrinsic

aging effects and fail to capture regulatory changes across different brain cell types and regions. Given the brain's cellular diversity, a cell-type-resolved analysis of chromatin aging is essential to distinguish intrinsic regulatory changes from shifts in cellular composition, especially since neurodegenerative diseases disproportionately affect specific brain regions and cell populations, such as dopaminergic neurons in the substantia nigra in Parkinson's disease,[13] oligodendrocytes in the white matter in multiple sclerosis,[14] and hippocampal neurons in Alzheimer's disease.[15]

Previous studies have characterized transcriptomic changes in aging at the single-cell level, including large-scale efforts such as Tabula Muris Senis,[2] which cataloged aging signatures across multiple tissues, and a recent brain-wide atlas of aging[3] that profiled 1.2 million neuronal and glial transcriptomes across the mouse brain. In addition to single-cell RNA sequencing (scRNA-seq), spatial transcriptomics has revealed white matter as particularly affected by aging.[16] These studies revealed that different cell types and spatial locations exhibit distinct transcriptional aging signatures. While transcriptomic atlases provide valuable insights, they alone do not capture the regulatory mechanisms driving transcriptional shifts.

Here, we present a comprehensive single-cell atlas of chromatin accessibility and transcriptional changes during brain aging, integrating single-cell assay for transposase-accessible chromatin using sequencing (ATAC-seq), RNA-seq, and spatial transcriptomics data across eight mouse brain regions involved in cognition, memory, emotional regulation, and neurodegenerative processes.[17] By resolving epigenomic changes at single-cell resolution, we uncover regulatory mechanisms that contribute to aging-associated transcriptional shifts and cellular dysfunction.

RESULTS

Single-nucleus multi-omic analysis of aging mouse brains

To determine how chromatin accessibility and transcriptional programs shift during aging, we profiled eight brain regions across three ages (2, 9, and 18 months) in adult mice using single-nucleus ATAC-seq (snATAC-seq), single-nucleus Multiome (ATAC-seq + RNA-seq), and multiplexed, error-robust RNA fluorescence *in situ* hybridization (MERFISH) (Table S1). For snATAC-seq, we profiled each brain region in 2 biological replicates, each containing pooled brain tissue dissected from 3–7 mice, of 9- and 18-month-old males while incorporating our previously reported 2-month-old mouse brain data.[18] For female samples, we generated single-nucleus 10× Multiome data, extending our analysis to both modalities (ATAC-seq and RNA-seq) from all three age groups. In total, we analyzed chromatin accessibility in 1,116,638 cells, RNA expression in 368,491 cells, and spatial transcriptomics in 500,353 cells, providing a comprehensive view of age-dependent gene regulation and cellular composition (Figures 1A, 1B, and S1A). We processed snATAC-seq data using SnapATAC2 and scRNA-seq + MERFISH data using Seurat.[19] Batch correction with Harmony[20] minimized batch effects between the male snATAC-seq and female 10× Multiome datasets (Figure S1B). Further integration across modalities and sexes revealed minimal batch effects and consistent cell-type distributions (Figures S1C–S1F).

Among 80 distinct cell types identified using marker genes and integration with a single-cell transcriptomic atlas of the adult mouse brain,[21] the most abundant populations were oligodendrocytes, dentate gyrus (DG) glutamatergic neurons, and striatal D12 medium spiny neurons (MSNs) (Figure S1G). Notably, three progenitor cell populations showed significant age-related declines in cell abundance: immature oligodendrocytes (IOLs); inhibitory immature neurons originating from the subventricular zone that migrate to the olfactory bulb, striatum, and cerebral cortex (OB-STR-CTX IMNs); and DG progenitors (Figures 1C and 1D). These declines were observed across snATAC-seq, Multiome, and MERFISH datasets and localized to canonical neurogenic niches in aged brains (Figures 2A–2D).

Chromatin accessibility remodeling with aging

We identified 881,231 open chromatin regions and candidate *cis*-regulatory elements (cCREs) across all cell types using MACS3[22] (STAR Methods; Figure S2A), 724,636 of which were previously reported in the young mouse brain.[23] A majority of cCREs were cell-type specific (Figure S2B). We assessed differential chromatin accessibility between 2- and 18-month-old samples using integrated data across sexes. We defined significant changes using an adjusted (adj.) $p < 0.01$ and fold changes (|log fold change| [|logFC|] > 0.5). This analysis revealed widespread chromatin remodeling with aging. At the most granular level, 88,555 cCREs exhibited significant increases in accessibility in at least one combination of cell type, region, and sex, with 30,994 unique to a single comparison. Conversely, 70,734 cCREs showed significant decreases, with 27,307 unique to a single combination. Some loci were recurrently altered across multiple n changes.[24] Strikingly, the most highly differential peaks across the genome were consistent between males and females, with several gene clusters—including the killer cell lectin-like receptor (*Klra*), secretoglobin (*Scgb*), olfactory receptor (*Olfr*), prostate and testis expressed (*Pate*), and protocadherin gamma (*Pcdhg*) gene families—alongside intergenic regions, showing strong upregulation in neuronal aging (Figures S3A and S3B).

To validate the biological authenticity of observed aging patterns across technologies, we performed within-sex aging analyses that eliminate potential cross-sex batch confounding. These analyses revealed strong correlations between male and female aging signatures (Figure S4), confirming that our integrated approach captures genuine biological patterns rather than technical artifacts.

To complement our chromatin accessibility analysis, we performed differential gene expression analysis using MAST, adjusting for brain region, mitochondrial percentage, ribosomal percentage, and replicate as latent variables.[25] This analysis revealed widespread transcriptional changes across glutamatergic, GABAergic, and non-neuronal cell types with aging (Figures S6A, S7A, and S8A; STAR Methods). Taken together, our analyses show that aging alters chromatin accessibility and transcriptional programs in a cell-type-specific manner in the mouse brain.

Loss of progenitor populations in aging brains

As shown above, three progenitor-like populations exhibit progressive declines in relative abundance across 2, 9, and 18 months (Figures 1D and 2A–2C). Among these, DG progenitors exhibit the most striking reduction, decreasing from ~3% abundance in 2-month-old brains to <0.01% in both the anterior hippocampus (AHC) and posterior hippocampus (PHC) (Figure 2D). These cells reside within one of the two major neurogenic niches in the adult brain, the DG, where they give rise to excitatory granule neurons. The other principal neurogenic niche, the subventricular zone (SVZ), produces inhibitory neurons that migrate to the olfactory bulb. In line with this, we identified a second declining population, olfactory bulb immature inhibitory neuron-like cells, annotated as OB-STR-CTX Inh IMNs.[21] These cells are primarily found in the nucleus accumbens (NAC), caudate putamen (CP), and hippocampus, comprising ~4% of cells at 2 months but declining with age at varying rates (Figure 2D). The third progenitor population showing a dramatic age-related decline is an intermediate cell type between oligodendrocyte progenitor cells and mature oligodendrocytes, known as IOLs. This population consistently decreases across brain regions, from ~2% to ~0.1% with aging, aligning with prior findings of impaired remyelination in the aging brain[26] (Figures 2C and 2D).

Recent studies suggest that progenitor cell exhaustion in aging is driven by chromatin changes, including loss of repressive histone marks and altered chromatin accessibility, rather than a simple failure of proliferation.[27] To determine whether chromatin changes accompany progenitor depletion, we analyzed age-differentially accessible CREs (cCREs) in progenitor cell populations across age groups. Motif enrichment analysis revealed a significant depletion of homeobox motifs in OB-STR-CTX Inh IMNs and Sox motifs in IOL cells, indicating dysregulation of cell-identity transcription factors (Figure 2E). In OB-STR-CTX Inh IMNs, differential accessibility analysis revealed a progressive shift in chromatin accessibility with aging, suggesting a gradual rather than abrupt epigenomic transition during aging (Figure 2F). Lhx2 emerged as the most significantly downregulated transcription factor in OB-STR-CTX Inh IMNs, with age-associated decreases in accessibility at Lhx2-motif sites (Figure 2G). Lhx2 is a key transcriptional regulator of neurogenic progenitors, maintaining their self-renewal capacity and delaying differentiation into mature neuronal or glial fates.[28,29] In embryonic and adult neural stem cells, Lhx2 prevents premature differentiation and supports ongoing neurogenesis, in part by directly activating downstream targets such as *Pax6*.[28,30] Consistent with this, differential gene expression analysis between 2- and 18-month-old samples revealed that *Pax6*, a direct target of Lhx2 and a key regulator of neurogenic lineage specification,[30] was significantly downregulated in both scRNA-seq and MERFISH data (adj. $p < 0.001$, ~11.7-fold reduction in expression) (Figure 2J). *Pax6* is crucial for neural fate specification, and its age-related depletion underscores the progressive decline of neurogenic potential. Gene Ontology (GO) pathway enrichment analysis of genes differentially expressed between the young 2- and 18-month-old samples revealed that those associated with learning, memory, and cell projection morphogenesis were downregulated with age (Figure 2I). Conversely, genes related to synapse organization were significantly upregulated in these progenitors (Figure 2I), suggesting that a subset of cells may be prematurely differentiating. While progenitor depletion is a well-documented feature of aging, the upregulation of synaptic

genes in the remaining OB-STR-CTX Inh IMN population may reflect a disruption in the balance between undifferentiated progenitors and early postmitotic neurons. This shift may be linked to the loss of Lhx2 and other homeobox transcription factors, which normally sustain the neurogenic program and suppress premature differentiation.[29] Together, these findings support a model in which age-related chromatin remodeling leads to the disruption of progenitor identity in OB-STR-CTX Inh IMNs, in part through the progressive loss of Lhx2 and *Pax6* transcriptional regulation.

Dysregulation of cell identity genes in glial cells during aging

Similar to the progenitor populations, we also observed widespread transcriptional and chromatin accessibility changes in oligodendrocytes, astrocytes, and microglia, which likely impact their ability to maintain brain homeostasis and support neuronal function. Dysfunction in these glial populations has been linked to neurodegenerative processes,[31] underscoring the importance of understanding their regulatory changes with age.

In oligodendrocytes, we identified 1,727 upregulated and 2,501 downregulated cCREs across aging (Figure S6A). Chromatin accessibility changes in oligodendrocytes were consistent across brain regions and sexes and progressed gradually from 2 to 18 months (Figure 3A). Like IOLs, mature oligodendrocytes exhibit a decline in the activity of Sox transcription factors, which are crucial for maintaining oligodendrocyte identity (Figures 2E and 3B).[32] Motif enrichment analysis revealed significant enrichment of Sox family and Creb5 motifs in downregulated cCREs, while KLF (Krüppel-like factors) and SP (specificity function) family motifs were enriched in upregulated peaks, marking a shift in transcription factor activity (Figures 3B and 3C). Differential gene expression analysis (Figure 3D) revealed a downregulation of genes related to myelin sheath formation and energy production, while genes associated with synaptic organization were enriched in upregulated genes (Figure 3E). Previous studies have shown that oligodendrocytes express synaptic genes, which participate in axon-myelin communication.[33] In this context, the upregulation of synaptic organization genes in aging oligodendrocytes may reflect an adaptive response to maintain axon-glial interactions as neural circuits change with age. On the other hand, the downregulation of myelination-related genes was evident across the 8 brain regions (Figures S5B and S5C). *Mal*, a gene that functions in the recruitment of myelin protein in oligodendrocytes,[34] is found to be significantly downregulated in oligodendrocytes from aged mice in both MERFISH and RNA-seq analyses (Figure 3H).

We linked these differential genes to key regulatory cCREs in oligodendrocytes using activity-by-contact (ABC) analysis.[36] We calculated ABC scores using the snm3C-seq contact data from our companion paper (Zeng et al.[35]) and the accessibility data from our work in matching cell types. We found that Sox10 was the most significantly enriched transcription factor motif within peaks linked to downregulated genes in aging oligodendrocytes (Figure 3G). Sox10 is a master regulator of oligodendrocyte lineage progression and myelin gene expression, playing a critical role in maintaining oligodendrocyte function and promoting myelination.[32] While Sox transcription factors are well established as essential regulators of oligodendrocyte development, our findings reveal that their downregulation in aging could contribute to the well-documented loss

of myelination in aged brains.[37,38] This suggests that, in addition to being critical for early oligodendrocyte differentiation, Sox factors are important in maintaining myelination throughout life, highlighting a previously underappreciated role for these transcription factors in aging-related myelin decline. Beyond transcription factor activity dysregulation and downregulation of important functions such as myelination, aging oligodendrocytes exhibit increased expression of genes involved in inflammatory and regulatory pathways, including the long noncoding RNA (lncRNA) *Neat1*, Parkinson's disease driver gene *Snca*, and inflammatory marker *Il33* (Figure 3F). These changes may reflect a shift in cellular state, such as increased responsiveness to neuronal and immune cues.

Similar to oligodendrocytes, astrocytes and microglia exhibit increased accessibility at enhancers linked to stress-responsive transcription factors during aging. For instance, astrocytes in the frontal cortex (FC) exhibit enrichment for ATF(Zf) motifs at age-gained cCREs (Figure S6B), while microglia, particularly from the AHC, exhibit enrichment for IRF8 motifs, suggestive of immune activation. Alongside the upregulation of genes such as Tnsfs8 and Ildr2 and the downregulation of classical microglial markers such as C1qa and Cst3, these findings are consistent with previously reported glial transcriptional shifts during aging.[1,7,39–41]

Upregulation of AP-1-mediated transcriptional programs in aging glutamatergic neurons

Glutamatergic neurons, responsible for excitatory signaling in the brain, also exhibit widespread chromatin and transcriptional changes during aging, with distinct regional vulnerabilities (Figure S8). In DG neurons, age-related chromatin remodeling exhibits clear regional specificity, with the AHC and PHC showing divergent patterns of accessibility changes. We identified 3,495 upregulated and 3,505 downregulated cCREs in aged DG neurons, with clusters of age-upregulated peaks enriched in the AHC, while a distinct set of peaks showed greater downregulation in the PHC (Figure 4A). Motif enrichment analysis highlights regional differences in transcription factor activity, with CTCF motifs preferentially enriched in age-upregulated cCREs in the AHC, suggesting altered chromatin looping and genome architecture in this region. Stress-responsive transcription factor complex AP-1 (activator protein 1) motifs are significantly upregulated in both brain regions (Figure 4B). Conversely, MEF2 motifs were strongly enriched in downregulated cCREs in the PHC, suggesting a regional loss of transcriptional programs involved in synaptic plasticity and neuronal maintenance. MEF2 transcription factors regulate activity-dependent synapse remodeling and neuronal survival.[40,42]

Genes involved in DNA damage response are upregulated in aging DG neurons, while genes involved in axonogenesis are downregulated (Figures 4D and 4E). ABC analysis reveals that open chromatin regions linked to age-upregulated genes in these neurons are enriched for AP-1 and CTCF motifs, while those associated with downregulated genes are enriched for NeuroG2 motifs (Figure 4F). This indicates a shift from developmental transcriptional programs toward stress-responsive regulatory networks during aging, with AP-1 motifs associated with aging-related gene expression changes. This is consistent with recent findings showing AP-1 redistribution to stress-responsive CREs, while cell identity transcription factor binding site occupancy declines.[7] These findings highlight the regional

specificity of chromatin remodeling in DG neurons, where the AHC exhibits stronger stress responses and chromatin reorganization, while the PHC experiences a greater loss of neurodevelopmental regulatory programs.

Beyond the hippocampus, glutamatergic neurons across multiple brain regions undergo extensive chromatin and transcriptional changes with aging. Motif enrichment analysis highlights an increase in open chromatin elements recognized by stress-responsive transcription factors, particularly KLF and AP-1, suggesting that aging is associated with enhanced stress adaptation in glutamatergic neurons (Figure S8B). Conversely, MEF2 and RFX motifs are enriched in downregulated cCREs across aging neurons, indicating a loss of transcription factor binding at sites critical for neuronal development and synaptic maintenance (Figure S8B). CTCF motifs show strong enrichment in age-upregulated peaks across multiple regions, including the FC, entorhinal cortex (ENT), and AHC, further supporting widespread chromatin remodeling during aging (Figure S8B). Gene set enrichment analysis (GSEA) reveals consistent downregulation of axonogenesis and oxidative phosphorylation pathways, suggesting a decline in synaptic plasticity and metabolic function across multiple glutamatergic neuron subtypes (Figures S12B and S13B). These transcriptional shifts align with previous findings that neuronal aging is marked by reduced bioenergetic capacity and neurogenesis.[3] Together, these findings demonstrate that glutamatergic neurons undergo significant age-related chromatin reorganization and transcriptional remodeling, with region-specific regulatory shifts in DG neurons and widespread stress responses across cortical regions.

Protocadherin locus derepression and chromatin remodeling in aging MSNs

D12 MSNs exhibit significant chromatin remodeling and transcriptional changes with aging (Figure S7A). These GABAergic neurons is present in the CP and NAC. We further identified clusters of cCREs that are upregulated to higher levels in the NAC and clusters of peaks more strongly downregulated in the CP (Figure S9A). RFX motifs, which are involved in neuronal function[43] and are broadly enriched in downregulated peaks of many neuronal subtypes, are enriched in upregulated peaks of the NAC (Figure S9B). AP-1 motifs show significant enrichment in upregulated peaks across both regions, as in glutamatergic neurons (Figures S9B and S8B), suggesting that these neurons experience particularly high levels of aging-related stress.

Genes related to cell junction organization were significantly enriched in upregulated genes in aging, including neuregulin (Nrg) family members and protocadherins such as *Pcdhgc5* (Figure S9C). One of the most striking chromatin changes in aging D12 MSNs is increased accessibility at the Pcdhg and protocadherin alpha (Pcdha) loci, gene clusters essential for neuronal self-recognition and synaptic organization.[44] While protocadherins exhibit differential expression across multiple cell types, D12 MSNs show the strongest alterations at this locus, present in both brain regions (Figure S9F). Notably, transcriptional upregulation within the Pcdhg cluster is largely intronic, suggesting that regulatory elements or noncoding RNAs within this region may be differentially expressed rather than the protein-coding genes themselves. Among these, *3222401L13Rik*, an lncRNA within the Pcdhg locus that has recently been implicated in aging astrocytes,[45] is upregulated across

multiple cell types. Chromatin conformation analyses (Zeng et al.[35]) show structural changes at this locus, revealing increased contact frequency within the loci and decreased interactions with upstream genomic regions (Figure S9E). These findings suggest that aging-induced chromatin reorganization in D12 MSNs may enhance protocadherin cluster activity while altering broader regulatory landscapes.

Heterochromatin destabilization, transposable element activation, and lncRNA dysregulation in aging brains

We next examined how heterochromatin domains and transposable elements (TEs) are affected during brain aging. In our previous work, we found that aging is accompanied by widespread chromatin remodeling, particularly at heterochromatin domains and TEs,[24] and aging neurons exhibit significant heterochromatin loss, particularly in cortical regions. With the increased resolution and broader scope of our current dataset spanning eight brain regions and multiple cell types, we now find that this phenomenon extends beyond neurons, with broad destabilization at putative heterochromatin observed across diverse glial and neuronal populations. However, this effect remains most pronounced in glutamatergic neurons, particularly in the FC, hippocampus, ENT, and amygdala, while the NAC, periaqueductal gray, and CP exhibit little to no change (Figure S10).

We overlapped age-associated differentially accessible regions and H3K9me3-marked domains based on ENCODE forebrain H3K9me3 chromatin immunoprecipitation sequencing (ChIP-seq) from postnatal day 0 mice.[46] Age-upregulated peaks were significantly enriched in these regions, particularly in glutamatergic neurons (Figure 5A, middle), consistent with prior observations of chromatin remodeling in aging neurons. TEs also showed increased accessibility across cell types (Figure 5A, right), with subfamilies such as IAPLTR3-int showing consistent patterns of activation (Figure S12C). An analysis including the 9-month intermediate time point confirmed that TE accessibility changes progressively through aging, with key families such as MuRRS-int and IAPLTR3-int showing consistent upregulation from 9 to 18 months (Figure S14). These trends were evident in both male and female mice (Figure S10B). Motif enrichment analysis revealed differentially upregulated regions within heterochromatin that were enriched for pioneer transcription factor AP-1 family (bZIP)[47] and CTCF motifs (Figure 5B).

Using Gaussian density scoring, a computational approach to identify genomic regions with significantly higher-than-expected concentrations of differential accessibility[24] (STAR Methods), we identified chromosomal aging hotspots across the genome. These hotspots were particularly upregulated in glutamatergic neurons, especially in cortical and hippocampal regions (Figure 5C). Notably, 47% of significantly upregulated hotspots overlap H3K9me3-marked domains, despite these regions covering only ~3% of the genome. This strong association between aging-associated accessibility gains and constitutive heterochromatin suggests a widespread remodeling of repressive chromatin compartments during aging. Many of these hotspots correspond to intergenic regions with TE activity, gene clusters that are typically repressed in mature neurons, and lncRNAs (Figure S3). Notably, lncRNAs were overrepresented among the most differentially expressed genes in aging, with over 50% of the top 100 upregulated genes in some cortical

neuron cell types belonging to this category (Figure 5G). One of the most prominent aging-associated hotspots is located at the start of chromosome 13, where accessibility gains were observed across five brain regions (Figure 5E). This region contains the lncRNA *Gm48530*, which was the most significantly upregulated gene in aging cortical neurons across the same five brain regions (Figure 5D). The hotspot also overlaps *IAPLTR3-int*, a TE element that exhibited increased accessibility in multiple cell types (Figures 5H and S12C). Together, this locus exhibited coordinated increases in chromatin accessibility, gene expression, and hypomethylation (Figure 5H), suggesting that age-related chromatin remodeling at heterochromatin domains may alter regulatory landscapes and lead to transcriptional activation.

Beyond autosomal hotspots, several aging-associated hotspots were found in the X chromosome in female samples (Figures S11A and S3). The most significant of these occurred at the Firre lncRNA locus, which exhibited continuous accessibility increases (Figure S11A). This finding aligns with previous reports linking aging to the loss of X chromosome inactivation.[48–50] Similarly, the lncRNA *Dxz4*, another key element involved in X chromosome organization, exhibited increased accessibility in aging neurons, suggesting that large-scale shifts in X-linked chromatin architecture may accompany aging (Figure S11A). In parallel, Xist and Tsix, two critical regulators of X chromosome inactivation, were among the most differentially upregulated genes across multiple female brain regions and cell types, especially in neurons, consistent with previous research (Figure S11C).[49] This could be a compensatory mechanism to counteract the possible loss of X chromosome inactivation we observe. Interestingly, while the *Firre* and *Dxz4* loci gained accessibility with age, the pseudoautosomal region at the end of the X chromosome, which typically escapes X inactivation, exhibited a striking loss of chromatin accessibility and gene expression in female mice (Figures S11A and S11B). The most affected region included *Erdr1* (*Gm47283*), which was the most consistently downregulated lncRNA in female brain aging across cell types and brain regions.

Taken together, our findings point to chromatin remodeling at putative heterochromatin regions, increased TE accessibility, and lncRNA dysregulation as key transcriptional and epigenomic features of aging in the brain. We note that genes involved in oxidative phosphorylation (Figures S13A and S13B) and heterochromatin maintenance (Figure S13C), including histone methyltransferases and chromatin remodeling factors, were among the most consistently downregulated across cell types. While these patterns may contribute to regulatory instability, further studies are needed to determine the causal role of heterochromatin dynamics in age-related functional decline.

DISCUSSION

We show here that aging is accompanied by widespread changes in chromatin accessibility and transcription factor activity across both glial and neuronal cell types in the mouse brain. Our single-cell epigenomic and transcriptomic analysis across eight brain regions further reveals master transcription factor loss, stress-induced reprogramming, and heterochromatin instability in the aging brain, extending recent transcriptomic aging atlases,[2,16,51] by providing the regulatory context underlying these transcriptional changes.

A central feature of aging revealed by our data is the progressive decline of lineage-defining transcription factors. In progenitor populations, reductions in *Lhx2* and *Pax6* likely contribute to impaired neurogenic capacity, consistent with well-documented age-related exhaustion of neural stem cells and reduced neurogenesis in the adult hippocampus and SVZ.[52–54] In oligodendrocytes, reduced *Sox* activity provides a regulatory basis for age-related myelin decline. In neurons, loss of *Mef2* and *NeuroG2* activity coincides with downregulation of axonogenesis and synaptic plasticity programs.

As developmental transcription factors decline, aging cells exhibit increased activation of stress-responsive transcriptional programs. We observe enrichment of AP-1 motifs in neurons, KLF motifs across multiple cell types, and IRF-family motifs in microglia, linking aging to inflammatory and stress-associated regulatory states. While AP-1 enrichment is a consistent feature of age-gained regulatory elements, future perturbation studies will be required to establish causal roles for these factors in aging phenotypes.

Another defining feature of brain aging is widespread heterochromatin destabilization, accompanied by TE activation and lncRNA upregulation. These findings align with accumulating evidence that heterochromatin maintenance is critical for longevity across species[6,55,56] and that interventions targeting chromatin structure can ameliorate aging phenotypes.[8,9,11] Age-associated accessibility gains at H3K9me3-marked domains are most pronounced in glutamatergic neurons but extend across multiple cell types. Female mouse brains also exhibit extensive X chromosome remodeling, including increased accessibility at heterochromatin-associated loci and reduced accessibility at pseudoautosomal regions, suggesting sex-specific epigenetic aging mechanisms.

Together, our findings support a model in which aging involves progressive erosion of epigenetic constraints that normally stabilize cell identity, leading to transcriptional drift toward stress-responsive states.[7,57] This regulatory instability may underlie age-related cognitive decline and neurodegeneration and highlights chromatin maintenance and transcription factor networks as potential targets for interventions aimed at preserving brain function during aging.

Limitations of the study

Sex-specific analyses are constrained by the use of different experimental platforms in males and females, limiting direct comparisons. This study profiles chromatin accessibility and transcriptional changes during brain aging but is limited to three time points, which may not fully resolve temporal dynamics.

RESOURCE AVAILABILITY

Lead contact

Requests for further information and resources should be directed to and will be fulfilled by the lead contact, Bing Ren (bren@nygenome.org).

Materials availability

This study did not generate new unique reagents.

Data and code availability

Raw sequencing data are available in the SRA under project SRA: PRJNA1248586, and processed data are deposited in GEO under accession GEO: GSE294772. The analysis code is available on GitHub at https://github.com/luisajamaral/aging_mouse_brain_code. Any additional information needed to reanalyze the data is available from the lead contact upon request.

STAR★METHODS

EXPERIMENTAL MODEL AND STUDY PARTICIPANT DETAILS

Mouse brain tissue: C57BL/6J male and female mice were purchased from the Jackson Laboratory at 7, 38 and 63 weeks of age and maintained in the Salk animal barrier facility on 12-h dark–light cycles with food *ad libitum* until brain extraction (housing conditions: temperature of 21–23°C, relative humidity of 61–63%). To standardize housing conditions, females were exposed to male bedding for three days prior to brain extraction. All animals were dissected between 1 and 5 pm to ensure similarity of circadian rhythm. Brains were extracted at 2, 9 or 18 months of age, sliced coronally at 600 μm and regions dissected in an ice-cold dissection buffer as previously described[61] according to the Allen Brain Reference Atlas CCF (version 3)[61](CCFv3). Dissected tissue corresponding to the same region (across the anterior posterior axis) from each animal was collected across brain slabs and stored at −80°C. For nuclei isolation, region pools from 3 to 14 animals were processed for each of 2–3 biological replicas per region. Comprehensive brain dissection metadata are provided in Table S1.

Institutional permission and oversight: All experimental procedures using live animals were performed at the Salk Institute, and were approved by the Animal Care and Use Committee (IACUC). The Salk Institute has approved Assurance from NIH Office of Protection from Research Risks (D16–00328).

Study design: Blinding and randomization were not performed during handling of the tissue samples. No statistical methods were used to predetermine sample sizes. The number of animals needed to obtain sufficient nuclei from each brain region to run single nuclei sequencing experiments was empirically determined. Two to three biological replicas were used for all single-cell epigenomic experiments to ensure reproducibility for large-scale projects.

Influence of sex: The study analyzed samples from both male and female mice. To validate the biological authenticity of observed aging patterns across technologies and eliminate potential cross-sex batch confounding, within-sex aging analyses were performed. These analyses revealed strong correlations between male and female aging signatures (e.g., oligodendrocytes: $r = 0.801$ for fold changes, $\rho = 0.497$ for signed significance; Figure S4), confirming that the integrated approach captures genuine biological patterns.

METHOD DETAILS

Nuclei isolation and dissection: Nuclei isolation was achieved following established protocols as previously described.[61] Additionally, all dissected regions were previously digitally registered into CCFv3 using ITK-SNAP[61] (v.4.0.0) at 25 μm resolution.

Single-nucleus ATAC-seq data generation: Nuclei were pelleted with a swinging bucket centrifuge (500g, 5 min, 4°C; 5920R, Eppendorf). Nuclei pellets were resuspended in 1 mL nuclei permeabilization buffer (1mM DTT (D9779, Sigma), 0.2% IGEPAL-CA630 (Sigma), 1X cOmplete EDTA-free protease inhibitor (05056489001, Roche) and 5% BSA (A7906, Sigma) in PBS) and pelleted again (500g, 5 min, 4°C; 5920R, Eppendorf). Nuclei were resuspended in 500 μL of tagmentation buffer (36.3 mM.

Tris-acetate, pH 7.8 (BP-152, Thermo Fisher Scientific), 72.6mM Potassium-acetate (P5708, Sigma), 12.1 mM Magnesium-acetate (M2545, Sigma), 17.6% DMF (DX1730, EMD Millipore) in molecular biology-grade water) and counted using a hemocytometer. Concentration was adjusted to 2000 nuclei/uL, and 2000 nuclei were dispensed into each well of a 96-well plate. For tagmentation, 1 μL of barcoded Tn5 transposomes were added using a BenchSmart 96 (Mettler Toledo, RRID:SCR_018093), mixed five times, and incubated for 60 min at 37°C with 500 rpm shaking. To inhibit the Tn5 reaction, 10 μL of 40 mM EDTA was added to each well with a BenchSmart 96 and mixed 5 times, then incubated at 37°C for 15 min with 500 rpm shaking. Next, added 20 μL 2x sort buffer (2% BSA, 2 mM EDTA in PBS), mix 5x and combine in a reagent reservoir. If processing two or more samples per day, tagmentation was performed with different sets of barcodes in separate 96 well plates. After tagmentation nuclei from individual plates were pooled together, stained nuclei suspension with 3 μM Draq7 (1:100, 7406, Cell Signaling). Sort 20 nuclei per well into eight 96-well plates (total of 768 wells, 15,360 nuclei per sample) containing 10.5 mL EB (25 pmol primer i7, 25 pmol primer i5, 200 ng BSA (Sigma). Preparation of sort plates and all downstream pipetting steps were performed on a Biomek i7 Automated Workstation. After addition of 1 μL 0.2%SDS (15553035, Thermo Fisher Scientific) to each well, samples were incubated at 55°C for 7 min with 500 rpm shaking. Next, 1 μL 12.5%Triton X-() was added to each well to quench the SDS. Next, 12.5 mL NEBNext High-Fidelity 2X ~ PCR Master Mix (M0541, NEB) were added and samples were PCR-amplified (72°C 5 min, 98°C 30 s, (98°C 10 s, 63°C 30 s, 72°C 60 s) X 12 cycles, held at 12°C). After PCR, contents in all wells were combined. Libraries were purified according to the MinElute PCR Purification Kit manual (Qiagen) using a vacuum manifold (QIAvac 24 plus, Qiagen) and size selection was performed with SPRI Beads (Beckmann Coulter, 0.55x and 1.5x). Libraries were purified one more time with SPRI Beads (Beckmann Coulter, 1.5x). Libraries were quantified using a Qubit dsDNA HS Assay Kit (Invitrogen) and the nucleosomal pattern was verified using a Tapestation (High Sensitivity D1000, Agilent). Libraries were sequenced on a NextSeq500 (Illumina) and NovaSeq6000 (Illumina) using custom sequencing primers with following read lengths: 50 + 10 + 12 + 50 (Read1 + Index1 + Index2 + Read2).

10× Multiome (snATAC + snRNA) data generation: Nuclei were pelleted with a swinging bucket centrifuge (1000g, 10 min, 4°C; 5920R, Eppendorf). Nuclei pellets were

resuspended in sort buffer (1% BSA, 2 μM 7-AAD, 1x cOmplete EDTA-free protease inhibitor and 1U/uL RNasin in PBS) and stained 10 min on ice. Nuclei were sorted, and 120,000 nuclei were collected in 90 μL of collection buffer (5% BSA and 5U/uL RNasin). Nuclei were centrifuged (500 × g for 5 min at 4°C), and resuspended in nuclei permeabilization buffer (1mM DTT (D9779, Sigma), 0.2% IGEPAL-CA630 (Sigma), 1X cOmplete EDTA-free protease inhibitor (05056489001, Roche) and 5% BSA (A7906, Sigma) in PBS) incubated on ice for 1 min. Added 900 μL wash buffer and and pelleted again (500g, 5 min, 4°C; 5920R, Eppendorf). The nuclei were resuspended in 10 μL of 1X Nuclei Buffer and counted using a hemocytometer. A total of 18,000 nuclei were loaded per tagmentation reaction loaded onto a Chromium Controller (10× Genomics) for downstream 10× Multiome ATAC and gene expression workflows. Final library concentration was assessed by Qubit dsDNA HS Assay Kit (Invitrogen) and fragment size was checked using Tapestation High Sensitivity D1000 (Agilent) to ensure that proper fragment sizes. Libraries were sequenced using the NextSeq500 and a NovaSeq6000 (Illumina).

snATAC-seq data processing: Reads were aligned to the mm10 reference genome using bowtie2 (v2.3)[62] with default parameters and cell barcodes were added as a BX tag in the bam file. Only primary alignments were kept. Then we removed duplicated read pairs with Picard. Only proper read pairs with insert size less than 2000 were kept for further analysis. From the filtered BAM files, we processed the data using SnapATAC2 (v 2.5.1),[19] following the official SnapATAC2 documentation. Barcode processing and fragment generation were performed, and doublets were removed using Scrublet.[63] Nuclei with fewer than 1,000 fragments, more than 100,000 fragments, or a TSS enrichment score below 5 were discarded. For female 10× Multiome samples, we processed the CellRanger output directly using SnapATAC2, ensuring consistency between modalities. Fragment files were imported, and doublets were identified and removed using SnapATAC2's built-in method. TSS enrichment scores were computed using SnapATAC2's function, and cells with fewer than 1,000 fragments, more than 15,000 fragments, or a TSS enrichment score below 5 were removed. Read counting and clustering were performed using a cell-by-bin matrix at 500-bp resolution, which was binarized for clustering. Bins overlapping the ENCODE[64] blacklist (mm10) were removed to eliminate problematic regions. Read coverage normalization was performed using a log10(count +1) transformation followed by Z score scaling, and bins with extreme Z-scores greater than 2 were filtered out. Feature selection was performed by retaining the top 700,000 most variable features. For dimensionality reduction, the Jaccard Index was computed, followed by diffusion maps for embedding. The top 20 eigenvectors were selected based on variance explained, and 20 nearest neighbors were computed per nucleus. The Leiden algorithm was applied for clustering, and clusters were annotated using known marker genes. Batch effects between male and female samples were corrected using Harmony (v1.2.3)[20] prior to clustering. Low-quality clusters, including those with low TSS enrichment or suspected doublets, were removed from downstream analysis.

snRNA-seq data processing: Single-nucleus RNA-seq (snRNA-seq) data were generated using the 10× Genomics Multiome platform and processed with Cellranger-arc v2.0.2 to generate raw gene expression matrices.[65] Doublets were identified and removed

using DoubletFinder from the Cell Ranger output for each sample.[66] Downstream analysis was performed using Seurat v5.0.0 in R. Individual samples were then merged into a single Seurat object. Quality control was applied to remove low-quality nuclei, filtering out cells with fewer than 500 or more than 6000 detected genes, and cells with >10% mitochondrial reads. Normalization was performed using the SCTransform (SCT) workflow, which models technical noise while preserving biological variation. Dimensionality reduction was carried out with PCA, and the top 30 components were used to compute a shared nearest neighbor (SNN) graph for clustering using the Leiden algorithm. UMAP was used for visualization. Following initial clustering, further manual filtering was applied to remove remaining doublets and low-quality subclusters. Specifically, subclusters containing >50% cells with low UMI counts or high doublet scores were excluded.

Cell type annotation via label transfer: Cell type annotation was performed using label transfer from a reference dataset generated by the Allen Brain Institute (10X V3).[21] A subsampled version of this dataset, retaining 500 cells per cluster, was used as a reference. Subclass labels were transferred using Seurat's label transfer framework with rpca. Labels were transferred for GABAergic, glutamatergic, and non-neuronal cell types separately. Each subcluster of our scRNA-seq data was assigned a label if more than 80% of the cells within that subcluster were consistently mapped to a single reference label. For ambiguous clusters where label transfer results were inconsistent, manual annotation was performed using marker gene expression profiles to ensure accurate classification. This approach resulted in the identification of 80 distinct cell types in the snRNA-seq dataset. Given that the data was 10× Multiome, these annotations were also available for the corresponding ATAC-seq data. We extended the labels to the male scATAC-seq data via our joint clustering of the data. Subclusters were assigned labels based on whether the majority of labeled nuclei —previously labeled through RNA-based annotation—mapped to a specific cell type. This ensured consistency in cell type annotation across both RNA and ATAC datasets.

MERFISH gene panel design: To investigate cell-type-specific and age-associated transcriptional changes in the mouse brain, we designed a customized MERFISH panel consisting of 500 genes. Gene selection was informed by single-cell and spatial transcriptomic datasets, focusing on both cellular identity and biological processes implicated in aging. The panel includes 328 genes selected as cell type markers, capturing major neuronal and glial subtypes across brain regions. Marker genes were derived from comprehensive single-cell RNA-seq atlases[18,67] and a MERFISH-based spatial atlas of the aging mouse brain.[16] From the latter, we prioritized genes with the highest variance across cells to ensure inclusion of the most informative spatial markers. To increase resolution for early neurogenic populations, we also included a focused subset of genes enriched in neural progenitor populations, such as radial glia-like cells and dentate gyrus progenitors. The remaining 172 genes were selected for their relevance to aging biology. These include genes differentially expressed with age in previous datasets, as well as genes involved in pathways such as chromatin remodeling, inflammation, oxidative stress, and circadian regulation. A subset of 24 genes was included based on prior evidence linking clock dysfunction to aging phenotypes.[68] MERFISH panel genes and their corresponding sources can be found in Table S2.

MERFISH tissue preparation and imaging: Brain slabs were embedded in OCT, rapidly frozen in isopentane and dry ice, and stored at −80°C until ready for slicing. Coronal sections (12 μm thick) were collected from OCT-embedded tissue using a Leica CM1950 cryostat at −20°C. Sections were immediately fixed in 4% paraformaldehyde (pre-warmed to 37°C) for 30 min, then permeabilized in 70% ethanol according to the manufacturer's instructions. Sample preparation, including probe hybridization and gel embedding, was performed using the Vizgen sample preparation kit (10400012) following the provided protocol. Imaging was conducted with a MERSCOPE 500 Gene Imaging kit (Vizgen, 10400006) on a MERSCOPE system (Vizgen).

MERFISH data preprocessing: Following the data processing performed by the Vizgen MERSCOPE, the MERFISH data was first re-segmented using CellPose[58] (v2.1.1). Using the segmentation pipeline defined by the CellSegmentation class of the mftools package, the CellPose'cyto-2' model was used to perform a 2D segmentation on the 3rd z-slice of the DAPI stain images. These new segmentation masks were then used to regenerate the cell by gene matrix for downstream analysis. The MERFISH datasets were initially filtered to remove cells with less than 5 genes detected and to remove genes found in less than 3 cells. The datasets across all age groups were concatenated and processed using common Scanpy[59] (v1.10.0) functions in Python (v3.10.14). The datasets were first normalized to have the same total transcripts per cell and then log scaled, followed by principal component analysis (PCA). The nearest neighbors distance matrix was calculated with n_neighbors = 30, then leiden clustering, PAGA, and UMAP were performed with default parameters. The combined object with 2 month, 9 month, and 18 month samples was then batch corrected using Scanpy's ComBat function. To perform a preliminary annotation of the processed MERFISH samples, the Allen Brain Cell Atlas 10Xv3 single-cell mouse brain dataset was used as a reference dataset.[21] The subclass level annotation was applied to the single-cell reference data, and this label was then transferred to the MERFISH data using the label_clusters function from the mftools package. The label_clusters function identifies the common genes between the MERFISH and reference data, then computes the mean z-scored expression of each cluster in the MERFISH and reference single-cell datasets. To transfer labels from the reference data to MERFISH, the Pearson correlation is computed between each MERFISH and reference cluster's expression profile, then the MERFISH cluster is assigned the label of its most correlated single-cell reference cluster. This resulted in 34 different cell type labels that were transferred to the MERFISH dataset as an initial set of annotations.

Label transfer between snRNA and MERFISH for annotation: To assign cell type annotations to our MERFISH single-cell transcriptomic data, we performed label transfer from a matched snRNA-seq dataset using Seurat. We first subsampled the snRNA-seq reference to reduce the overrepresentation of large clusters, capping the maximum number of cells per annotated cluster at 2,000. Both the snRNA-seq and MERFISH datasets were normalized using SCTransform, and transfer anchors were computed using canonical correlation analysis (CCA) with the top 45 dimensions and all available genes (FindTransferAnchors, reduction = "cca"). Labels from the RNA-seq data (celltype_final) were transferred using TransferData, generating a predicted label and a confidence score

(prediction.score.max) for each MERFISH cell. To mitigate potential noise and improve robustness, we refined the transferred labels through subclustering. Each MERFISH cluster sub-clustered at higher resolution (FindClusters, resolution = 2) following PCA-based preprocessing. For each resulting subcluster, we determined the majority predicted label based on cells with high confidence (score >0.85). Any ambiguous subclusters were removed. For both modalities, gene expression was aggregated across cells of the same cell type using Seurat's AggregateExpression() function with centered log-ratio (CLR) normalization. The CLR transformation was applied per cell to adjust for differences in sequencing depth and compositional effects. For the RNA-seq data, gene expression values were further normalized by gene length to account for transcript length bias, yielding RPKM-like units based on CLR-normalized counts. Pearson correlation was computed across shared genes and cell types between the RNA-seq and MERFISH aggregated matrices.

QUANTIFICATION AND STATISTICAL ANALYSIS

Statistical details of experiments: Data are typically represented as mean values (e.g., in bar plots or aggregate accessibility plots). For all figures presenting pooled data, error bars (if present) represent the Standard Error of the Mean (SEM) or Standard Deviation (SD) as indicated in the figure. Unless otherwise specified, asterisks denote statistical significance as determined by the appropriate statistical test (likelihood ratio test for differential expression/accessibility, Wilcoxon rank-sum test for cell proportions, or HOMER for motif enrichment). Statistical details of experiments, including the statistical tests used, exact value of n, definition of center, and dispersion and precision measures, are included within the relevant sections of the STAR Methods(e.g., differential gene expression analysis, peak calling and differential accessibility analysis) and can be found in the associated figures, figure legends, and results section of the manuscript.

- **N represents (Sample Sizes):**
- **Animals:** Region pools from 3 to 14 animals were processed for each of 2–3 biological replicas per region.
- **Cells/Nuclei:** In total, the study analyzed chromatin accessibility in **1,116,638** cells, RNA expression in **368,491** cells, and spatial transcriptomics in **500,353** cells.
- **Statistical Tests and Corrections Used:**
- **Differential Gene Expression:** MAST (likelihood ratio tests).
- **Differential Accessibility/TEs:** Likelihood ratio tests (via DESeq2).
- **Cell Proportion Changes:** Wilcoxon rank-sum test.
- **Multiple Comparisons:** Benjamini-Hochberg correction was used to adjust p-values.
- **Concordance:** Pearson correlation (for within-sex aging signature analysis).
- **Key Quantification and Precision Measures:**

- **Definition of Center:** Mean (e.g., for calculating aggregated motif accessibility, ABC scores, $\log_2$ fold changes).
- **Significance Thresholds (Dispersion/Precision):**
- **Adjusted p-value:** < 0.01 (general significance cutoff).
- **q-value:** 0.01 (for MACS3 peak calling).
- **$\mathbf{Log_2}$ Fold Change (|logFC|):** > 0.5 (differential chromatin accessibility); >0.25 (differential gene expression).
- ***Z* score** (for normalized accessibility heatmaps).
- **Statistical Software:** R packages used include Seurat (v5.0.0), MAST (v1.28.0), clusterProfiler (v4.1), and smoother (v1.3). Python packages include Scanpy (v1.10.0) and SnapATAC2 (v2.5.1). Other software includes MACS3 (v3.0.0), HOMER (v 4.11), DESeq2 (v1.42.0), bowtie2 (v2.3), BWA, SICER (v1.0), scTE (v 1.0), and SoloTE (v1.09).

Differential gene expression analysis: Differential gene expression analysis was conducted using MAST[25] (v1.28.0) within Seurat (v5.0.0), incorporating latent variables to account for percent mitochondrial reads, percent ribosomal reads, replicate, and brain region where necessary. Statistical significance was determined using likelihood ratio tests, and multiple comparisons were adjusted using the Benjamini-Hochberg correction. Genes were considered differentially expressed if they met a log2 fold-change of 0.25 and an adjusted *p*-value <0.01. Statistical power for detecting differential changes varies across cell types due to differences in cell numbers, cCRE complexity, and baseline accessibility variance. Direct comparisons of effect sizes across cell types were avoided to prevent overinterpretation of these technical factors.

Pathway enrichment analysis: Pathway enrichment analysis was performed using clusterProfiler[69] on significantly upregulated and downregulated genes with all genes used in the DEG analysis as background (genes expressed in >1% of cells).

Peak calling and differential accessibility analysis: Peak calling and differential accessibility analysis were performed using SnapATAC2.[19] For peak calling, MACS3 (v3.0.0) was run on individual cell types using the snap.tl.macs3 function. Peaks were called separately for each cell type and age group using a q-value threshold of 0.01, with additional filtering against the ENCODE mm10 blacklist. To ensure robust peak detection, replicate-specific peaks were discarded. To identify differentially accessible regions (DARs), comparisons were made between 2-month-old and 18-month-old nuclei within each cell type. Peaks were filtered to include only those detected in at least 1% of cells in either age group. Differential testing was performed using snap.tl.diff_test, with a minimum log2 fold change of 0.25 and a significance threshold of adjusted *p*-value <0.01. Up- and downregulated peaks were extracted and saved as BED files for downstream analysis. For visualization, aggregated peak matrices were generated for each cell type, region, and age group, normalized to reads per million (RPM).

Motif enrichment analysis: Motif enrichment analysis was performed using HOMER (v 4.11)[60] for the age-differential peaks in each cell type, with non-differential peaks as the background and default parameters.

Overlap with histone marks: We used bedtools intersect -c to overlap all called peaks for each cell type with H3K9me3 data from ENCODE.[46] H3K9me3 data from the forebrain were re-aligned to mm10 genome using BWA[70] without mapping quality filter (in order not to lose any reads aligning to repetitive elements), and peaks were re-called using SICER (v1.0)[71] on both ChIP-seq and input libraries, as described in.[24]

Linking genes to cCREs via ABC score: To associate genes with putative regulatory elements, we employed the Activity-By-Contact (ABC) model, which integrates chromatin accessibility, histone modifications, and 3D chromatin interactions to predict enhancer-gene links. The ABC score was calculated following the framework described by Fulco et al.,[36] using open chromatin peaks as candidate *cis*-regulatory elements (cCREs).

Gaussian smoothing for hotspot identification: We used the R package smoother to perform Gaussian smoothing on the number of differentially accessible regions (DARs) ($p < 0.01$, |log2 fold change| > 1) within each 100 kb region of the genome. A smoothing window length of 20 bins (~2.1 Mb span) was applied to account for local clustering of accessibility changes. Regions of the genome with a high concentration of DARs within a short distance were assigned higher Gaussian smoothing scores, and hotspots were defined as bins with smoothing scores in the top 1%, corresponding to a threshold of 0.2.

Quantifying transposable elements (TEs) accessibility and expression

- **TE Accessibility:** scTE[72] (v 1.0) was used to build a genome index for the alignment of reads to genes (gencode vM21) and TEs (rmsk mm10) using scTE_build. The scTE command was used to map reads from the BAM files to transposable element families, generating a cell by feature read count matrix. A pseudo-bulk count table fo TE subfamilies was generated by summing reads from cells of the same cell type, age and biological replicate for each feature. Age-differential TEs for each cell type were then identified by DESeq2[73] (v1.42.0) between 18-month and 2-month datasets using the likelihood ratio test. Additional analysis comparing 9-month to 18-month samples confirmed the progressive nature of TE activation during aging (Figure S14).
- **TE Expression:** SoloTE[74] (v1.09) was used to count reads at TE elements and genes directly from the Cellranger output, generating a Seurat object that contained the gene and TE count matrix. A pseudo-bulk count table for both genes and TEs was generated by summing reads from cells of the same cell type, age and biological replicate for each feature. Age-differential genes and TEs for each cell type were then identified by DESeq2[73] between 18-month and 2-month datasets using the likelihood ratio test.

Supplementary Material

Refer to Web version on PubMed Central for supplementary material.

ACKNOWLEDGMENTS

This work was supported by National Institutes of Health (NIH) grant 5R01AG066018 to B.R., M.M.B., and J.R.E.

REFERENCES

1. Mattson MP, and Arumugam TV (2018). Hallmarks of brain aging: Adaptive and pathological modification by metabolic states. Cell Metab. 27, 1176–1199. [PubMed: 29874566]
2. Almanzar N, Antony J, Baghel AS, Bakerman I, Bansal I, Barres BA, Beachy PA, Berdnik D, Bilen B, Brownfield D, et al. (2020). A single-cell transcriptomic atlas characterizes ageing tissues in the mouse. Nature 583, 590–595. [PubMed: 32669714]
3. Jin K, Yao Z, van Velthoven CTJ, Kaplan ES, Glattfelder K, Barlow ST, Boyer G, Carey D, Casper T, Chakka AB, et al. (2025). Brain-wide cell-type-specific transcriptomic signatures of healthy ageing in mice. Nature 638, 182–196. [PubMed: 39743592]
4. Klemm SL, Shipony Z, and Greenleaf WJ (2019). Chromatin accessibility and the regulatory epigenome. Nat. Rev. Genet. 20, 207–220. [PubMed: 30675018]
5. López-Otín C, Blasco MA, Partridge L, Serrano M, and Kroemer G (2023). Hallmarks of aging: An expanding universe. Cell 186, 243–278. [PubMed: 36599349]
6. Wang K, Liu H, Hu Q, Wang L, Liu J, Zheng Z, Zhang W, Ren J, Zhu F, and Liu G-H (2022). Epigenetic regulation of aging: implications for interventions of aging and diseases. Signal Transduct. Target. Ther. 7, 374. [PubMed: 36336680]
7. Patrick R, Naval-Sanchez M, Deshpande N, Huang Y, Zhang J, Chen X, Yang Y, Tiwari K, Esmaeili M, Tran M, et al. (2024). The activity of early-life gene regulatory elements is hijacked in aging through pervasive AP-1-linked chromatin opening. Cell Metab. 36, 1858–1881.e23. [PubMed: 38959897]
8. Lu Y, Brommer B, Tian X, Krishnan A, Meer M, Wang C, Vera DL, Zeng Q, Yu D, Bonkowski MS, et al. (2020). Reprogramming to recover youthful epigenetic information and restore vision. Nature 588, 124–129. [PubMed: 33268865]
9. Roichman A, Elhanati S, Aon MA, Abramovich I, Di Francesco A, Shahar Y, Avivi MY, Shurgi M, Rubinstein A, Wiesner Y, et al. (2021). Restoration of energy homeostasis by SIRT6 extends healthy lifespan. Nat. Commun. 12, 3208. [PubMed: 34050173]
10. Akter R, Afrose A, Rahman MR, Chowdhury R, Nirzhor SSR, Khan RI, and Kabir MT (2021). A Comprehensive Analysis into the Therapeutic Application of Natural Products as SIRT6 Modulators in Alzheimer's Disease, Aging, Cancer, Inflammation, and Diabetes. Int. J. Mol. Sci. 22, 4180. [PubMed: 33920726]
11. Liu B, Wang Z, Zhang L, Ghosh S, Zheng H, and Zhou Z (2013). Depleting the methyltransferase Suv39h1 improves DNA repair and extends lifespan in a progeria mouse model. Nat. Commun. 4, 1868. [PubMed: 23695662]
12. Garcez ML, de Carvalho CA, Mina F, Bellettini-Santos T, Schiavo GL, da Silva S, Campos ACBF, Varela RB, Valvassori SS, Damiani AP, et al. (2018). Sodium butyrate improves memory and modulates the activity of histone deacetylases in aged rats after the administration of d-galactose. Exp. Gerontol. 113, 209–217. [PubMed: 30304709]
13. Balzano T, del Rey NL-G, Esteban-García N, Reinares-Sebastián A, Pineda-Pardo JA, Trigo-Damas I, Obeso JA, and Blesa J (2024). Neurovascular and immune factors of vulnerability of substantia nigra dopaminergic neurons in non-human primates. npj Parkinson's Dis. 10, 1–11. [PubMed: 38167744]
14. Ozawa K, Suchanek G, Breitschopf H, Brück W, Budka H, Jellinger K, and Lassmann H (1994). Patterns of oligodendroglia pathology in multiple sclerosis. Brain 117, 1311–1322. [PubMed: 7820568]
15. Rao YL, Ganaraja B, Murlimanju BV, Joy T, Krishnamurthy A, and Agrawal A (2022). Hippocampus and its involvement in Alzheimer's disease: a review. Biotech 12, 55.
16. Allen WE, Blosser TR, Sullivan ZA, Dulac C, and Zhuang X (2023). Molecular and spatial signatures of mouse brain aging at single-cell resolution. Cell 186, 194–208.e18. [PubMed: 36580914]

17. Jagust W (2013). Vulnerable Neural Systems and the Borderland of Brain Aging and Neurodegeneration. Neuron 77, 219–234. [PubMed: 23352159]

18. Li YE, Preissl S, Hou X, Zhang Z, Zhang K, Qiu Y, Poirion OB, Li B, Chiou J, Liu H, et al. (2021). An atlas of gene regulatory elements in adult mouse cerebrum. Nature 598, 129–136. [PubMed: 34616068]

19. Zhang K, Zemke NR, Armand EJ, and Ren B (2024). A fast, scalable and versatile tool for analysis of single-cell omics data. Nat. Methods 21, 217–227. [PubMed: 38191932]

20. Korsunsky I, Millard N, Fan J, Slowikowski K, Zhang F, Wei K, Baglaenko Y, Brenner M, Loh P-R, and Raychaudhuri S (2019). Fast, sensitive and accurate integration of single-cell data with Harmony. Nat. Methods 16, 1289–1296. [PubMed: 31740819]

21. Yao Z, van Velthoven CTJ, Kunst M, Zhang M, McMillen D, Lee C, Jung W, Goldy J, Abdelhak A, Aitken M, et al. (2023). A high-resolution transcriptomic and spatial atlas of cell types in the whole mouse brain. Nature 624, 317–332. [PubMed: 38092916]

22. Zhang Y, Liu T, Meyer CA, Eeckhoute J, Johnson DS, Bernstein BE, Nusbaum C, Myers RM, Brown M, Li W, and Liu XS (2008). Model-based analysis of ChIP-Seq (MACS). Genome Biol. 9, R137. [PubMed: 18798982]

23. Zu S, Li YE, Wang K, Armand EJ, Mamde S, Amaral ML, Wang Y, Chu A, Xie Y, Miller M, et al. (2023). Single-cell analysis of chromatin accessibility in the adult mouse brain. Nature 624, 378–389. [PubMed: 38092917]

24. Zhang Y, Amaral ML, Zhu C, Grieco SF, Hou X, Lin L, Buchanan J, Tong L, Preissl S, Xu X, and Ren B (2022). Single-cell epigenome analysis reveals age-associated decay of heterochromatin domains in excitatory neurons in the mouse brain. Cell Res. 32, 1008–1021. [PubMed: 36207411]

25. Finak G, McDavid A, Yajima M, Deng J, Gersuk V, Shalek AK, Slichter CK, Miller HW, McElrath MJ, Prlic M, et al. (2015). MAST: a flexible statistical framework for assessing transcriptional changes and characterizing heterogeneity in single-cell RNA sequencing data. Genome Biol. 16, 278. [PubMed: 26653891]

26. Peters A (2002). The effects of normal aging on myelin and nerve fibers: a review. J. Neurocytol. 31, 581–593. [PubMed: 14501200]

27. Sun D, Luo M, Jeong M, Rodriguez B, Xia Z, Hannah R, Wang H, Le T, Faull KF, Chen R, et al. (2014). Epigenomic profiling of young and aged HSCs reveals concerted changes during aging that reinforce self-renewal. Cell Stem Cell 14, 673–688. [PubMed: 24792119]

28. Hsu LC-L, Nam S, Cui Y, Chang C-P, Wang C-F, Kuo H-C, Touboul JD, and Chou S-J (2015). Lhx2 regulates the timing of β-catenin-dependent cortical neurogenesis. Proc. Natl. Acad. Sci. USA 112, 12199–12204. [PubMed: 26371318]

29. Subramanian L, Sarkar A, Shetty AS, Muralidharan B, Padmanabhan H, Piper M, Monuki ES, Bach I, Gronostajski RM, Richards LJ, and Tole S (2011). Transcription factor Lhx2 is necessary and sufficient to suppress astrogliogenesis and promote neurogenesis in the developing hippocampus. Proc. Natl. Acad. Sci. USA 108, E265–E274. [PubMed: 21690374]

30. Hou P-S, Chuang C-Y, Kao C-F, Chou S-J, Stone L, Ho H-N, Chien C-L, and Kuo H-C (2013). LHX2 regulates the neural differentiation of human embryonic stem cells via transcriptional modulation of PAX6 and CER1. Nucleic Acids Res. 41, 7753–7770. [PubMed: 23804753]

31. Sheeler C, Rosa J-G, Ferro A, McAdams B, Borgenheimer E, and Cvetanovic M (2020). Glia in Neurodegeneration: The Housekeeper, the Defender and the Perpetrator. Int. J. Mol. Sci. 21, 9188. [PubMed: 33276471]

32. Stolt CC, Rehberg S, Ader M, Lommes P, Riethmacher D, Schachner M, Bartsch U, and Wegner M (2002). Terminal differentiation of myelin-forming oligodendrocytes depends on the transcription factor Sox10. Genes Dev. 16, 165–170. [PubMed: 11799060]

33. Hughes AN, and Appel B (2019). Oligodendrocytes express synaptic proteins that modulate myelin sheath formation. Nat. Commun. 10, 4125. [PubMed: 31511515]

34. Bijlard M, de Jonge JC, Klunder B, Nomden A, Hoekstra D, and Baron W (2016). MAL is a regulator of the recruitment of myelin protein PLP to membrane microdomains. PLoS One 11, e0155317. [PubMed: 27171274]

35. Zeng Q, Tian W, Klein A, Bartlett A, Liu H, Nery JR, Castanon RG, Osteen J, Johnson ND, Wang W, et al. (2025). Cell-type-specific transposable element demethylation and TAD remodeling in the aging mouse brain. Preprint at bioRxiv. 10.1101/2025.04.21.648266.
36. Fulco CP, Nasser J, Jones TR, Munson G, Bergman DT, Subramanian V, Grossman SR, Anyoha R, Doughty BR, Patwardhan TA, et al. (2019). Activity-by-contact model of enhancer–promoter regulation from thousands of CRISPR perturbations. Nat. Genet. 51, 1664–1669. [PubMed: 31784727]
37. Gong Z, Bilgel M, Kiely M, Triebswetter C, Ferrucci L, Resnick SM, Spencer RG, and Bouhrara M (2023). Lower myelin content is associated with more rapid cognitive decline among cognitively unimpaired individuals. Alzheimer's Dement. 19, 3098–3107. [PubMed: 36720000]
38. Ibañez S, Sengupta N, Luebke JI, Wimmer K, and Weaver CM (2024). Myelin dystrophy in the aging prefrontal cortex leads to impaired signal transmission and working memory decline: a multiscale computational study. eLife 12. 10.7554/eLife.90964.2.
39. Clarke LE, Liddelow SA, Chakraborty C, Münch AE, Heiman M, and Barres BA (2018). Normal aging induces A1-like astrocyte reactivity. Proc. Natl. Acad. Sci. USA 115, E1896–E1905. 10.1073/pnas.1800165115. [PubMed: 29437957]
40. Li X, Li Y, Jin Y, Zhang Y, Wu J, Xu Z, Huang Y, Cai L, Gao S, Liu T, et al. (2023). Transcriptional and epigenetic decoding of the microglial aging process. Nat. Aging 3, 1288–1311. [PubMed: 37697166]
41. Kaya T, Mattugini N, Liu L, Ji H, Cantuti-Castelvetri L, Wu J, Schifferer M, Groh J, Martini R, Besson-Girard S, et al. (2022). CD8+ T cells induce interferon-responsive oligodendrocytes and microglia in white matter aging. Nat. Neurosci. 25, 1446–1457. [PubMed: 36280798]
42. Flavell SW, Cowan CW, Kim T-K, Greer PL, Lin Y, Paradis S, Griffith EC, Hu LS, Chen C, and Greenberg ME (2006). Activity-dependent regulation of MEF2 transcription factors suppresses excitatory synapse number. Science 311, 1008–1012. [PubMed: 16484497]
43. Choi W, Choe MS, Kim SM, Kim SJ, Lee J, Lee Y, Lee S-M, Dho SH, Lee M-Y, and Kim LK (2024). RFX4 is an intrinsic factor for neuronal differentiation through induction of proneural genes POU3F2 and NEUROD1. Cell. Mol. Life Sci. 81, 99. [PubMed: 38386071]
44. Flaherty E, and Maniatis T (2020). The role of clustered protocadherins in neurodevelopment and neuropsychiatric diseases. Curr. Opin. Genet. Dev. 65, 144–150. [PubMed: 32679536]
45. Schröder S, Sakib MS, Krüger DM, Pena T, Burkhardt S, Schütz A-L, Sananbenesi F, and Fischer A (2025). LncRNA 3222401L13Rik Is Upregulated in Aging Astrocytes and Regulates Neuronal Support Function Through Interaction with Npas3 Non-Coding. RNA 11, 2.
46. He Y, Hariharan M, Gorkin DU, Dickel DE, Luo C, Castanon RG, Nery JR, Lee AY, Zhao Y, Huang H, et al. (2020). Spatiotemporal DNA methylome dynamics of the developing mouse fetus. Nature 583, 752–759. [PubMed: 32728242]
47. Wolf BK, Zhao Y, McCray A, Hawk WH, Deary LT, Sugiarto NW, LaCroix IS, Gerber SA, Cheng C, and Wang X (2023). Cooperation of chromatin remodeling SWI/SNF complex and pioneer factor AP-1 shapes 3D enhancer landscapes. Nat. Struct. Mol. Biol. 30, 10–21. [PubMed: 36522426]
48. Wen X, Luo Z, Zhao W, Calandrelli R, Nguyen TC, Wan X, Charles Richard JL, and Zhong S (2024). Single-cell multiplex chromatin and RNA interactions in ageing human brain. Nature 628, 648–656. [PubMed: 38538789]
49. Hajdarovic KH, Yu D, Hassell L-A, Evans S, Packer S, Neretti N, and Webb AE (2022). Single-cell analysis of the aging female mouse hypothalamus. Nat. Aging 2, 662–678. [PubMed: 36285248]
50. Abdulai-Saiku S, Gupta S, Wang D, Marino F, Moreno AJ, Huang Y, Srivastava D, Panning B, and Dubal DB (2025). The maternal X chromosome affects cognition and brain ageing in female mice. Nature 638, 152–159. [PubMed: 39843739]
51. Hahn O, Foltz AG, Atkins M, Kedir B, Moran-Losada P, Guldner IH, Munson C, Kern F, Pálovics R, Lu N, et al. (2023). Atlas of the aging mouse brain reveals white matter as vulnerable foci. Cell 186, 4117–4133.e22. [PubMed: 37591239]

52. Encinas JM, Michurina TV, Peunova N, Park J-H, Tordo J, Peterson DA, Fishell G, Koulakov A, and Enikolopov G (2011). Division-coupled astrocytic differentiation and age-related depletion of neural stem cells in the adult hippocampus. Cell Stem Cell 8, 566–579. [PubMed: 21549330]

53. Molofsky AV, Slutsky SG, Joseph NM, He S, Pardal R, Krishnamurthy J, Sharpless NE, and Morrison SJ (2006). Increasing p16INK4a expression decreases forebrain progenitors and neurogenesis during ageing. Nature 443, 448–452. [PubMed: 16957738]

54. Kalamakis G, Brüne D, Ravichandran S, Bolz J, Fan W, Ziebell F, Stiehl T, Catalá-Martinez F, Kupke J, Zhao S, et al. (2019). Quiescence modulates stem cell maintenance and regenerative capacity in the aging brain. Cell 176, 1407–1419.e14. [PubMed: 30827680]

55. Tsurumi A, and Li WX (2012). Global heterochromatin loss: a unifying theory of aging? Epigenetics 7, 680–688. [PubMed: 22647267]

56. Scaffidi P, and Misteli T (2006). Lamin A-dependent nuclear defects in human aging. Science 312, 1059–1063. [PubMed: 16645051]

57. Yang J-H, Hayano M, Griffin PT, Amorim JA, Bonkowski MS, Apostolides JK, Salfati EL, Blanchette M, Munding EM, Bhakta M, et al. (2021). Loss of epigenetic information as a cause of mammalian aging. Cell 186, 305–326.e27. 10.1016/j.cell.2022.12.027.

58. Stringer C, Wang T, Michaelos M, and Pachitariu M (2021). Cellpose: a generalist algorithm for cellular segmentation. Nat. Methods 18, 100–106. [PubMed: 33318659]

59. Wolf FA, Angerer P, and Theis FJ (2018). SCANPY: large-scale single-cell gene expression data analysis. Genome Biol. 19, 15. [PubMed: 29409532]

60. Heinz S, Benner C, Spann N, Bertolino E, Lin YC, Laslo P, Cheng JX, Murre C, Singh H, and Glass CK (2010). Simple Combinations of Lineage-Determining Transcription Factors Prime \textitcis-Regulatory Elements Required for Macrophage and B Cell Identities. Mol. Cell 38, 576–589. [PubMed: 20513432]

61. Liu H, Zeng Q, Zhou J, Bartlett A, Wang B-A, Berube P, Tian W, Kenworthy M, Altshul J, Nery JR, et al. (2023). Single-cell DNA methylome and 3D multi-omic atlas of the adult mouse brain. Nature 624, 366–377. [PubMed: 38092913]

62. Langmead B, and Salzberg SL (2012). Fast gapped-read alignment with Bowtie 2. Nat. Methods 9, 357–359. [PubMed: 22388286]

63. Wolock SL, Lopez R, and Klein AM (2019). Scrublet: Computational identification of cell Doublets in Single-cell transcriptomic data. Cell Syst. 8, 281–291.e9. [PubMed: 30954476]

64. ENCODE Project Consortium (2004). The ENCODE (ENCyclopedia Of DNA elements) Project. Science 306, 636–640. [PubMed: 15499007]

65. Zheng GXY, Terry JM, Belgrader P, Ryvkin P, Bent ZW, Wilson R, Ziraldo SB, Wheeler TD, McDermott GP, Zhu J, et al. (2017). Massively parallel digital transcriptional profiling of single cells. Nat. Commun. 8, 14049. [PubMed: 28091601]

66. McGinnis CS, Murrow LM, and Gartner ZJ (2019). DoubletFinder: Doublet Detection in Single-Cell RNA Sequencing Data Using Artificial Nearest Neighbors. Cell Syst. 8, 329–337.e4. [PubMed: 30954475]

67. Zeisel A, Hochgerner H, Lönnerberg P, Johnsson A, Memic F, van der Zwan J, Häring M, Braun E, Borm LE, La Manno G, et al. (2018). Molecular architecture of the mouse nervous system. Cell 174, 999–1014.e22. [PubMed: 30096314]

68. Buckley MT, Sun ED, George BM, Liu L, Schaum N, Xu L, Reyes JM, Goodell MA, Weissman IL, Wyss-Coray T, et al. (2023). Cell-type-specific aging clocks to quantify aging and rejuvenation in neurogenic regions of the brain. Nat. Aging 3, 121–137. [PubMed: 37118510]

69. Xu S, Hu E, Cai Y, Xie Z, Luo X, Zhan L, Tang W, Wang Q, Liu B, Wang R, et al. (2024). Using clusterProfiler to characterize multiomics data. Nat. Protoc. 19, 3292–3320. [PubMed: 39019974]

70. Li H, and Durbin R (2009). Fast and accurate short read alignment with Burrows–Wheeler transform. Bioinformatics 25, 1754–1760. [PubMed: 19451168]

71. Zang C, Schones DE, Zeng C, Cui K, Zhao K, and Peng W (2009). A clustering approach for identification of enriched domains from histone modification ChIP-Seq data. Bioinformatics 25, 1952–1958. [PubMed: 19505939]

72. He J, Babarinde IA, Sun L, Xu S, Chen R, Shi J, Wei Y, Li Y, Ma G, Zhuang Q, et al. (2021). Identifying transposable element expression dynamics and heterogeneity during development

at the single-cell level with a processing pipeline scTE. Nat. Commun. 12, 1456. [PubMed: 33674594]

73. Love MI, Huber W, and Anders S (2014). Moderated estimation of fold change and dispersion for RNA-seq data with DESeq2. Genome Biol. 15, 550. [PubMed: 25516281]
74. Rodríguez-Quiroz R, and Valdebenito-Maturana B (2022). SoloTE for improved analysis of transposable elements in single-cell RNA-Seq data using locus-specific expression. Commun. Biol. 5, 1–12. [PubMed: 34987157]

Highlights

- Integrated single-cell and spatial atlas maps regulatory changes in aging mouse brain
- Loss of neural and glial progenitors coincides with disrupted developmental regulators
- Transcription factor dysfunction drives neuronal and glial identity drift with age
- Heterochromatin destabilization activates transposable elements and noncoding RNAs

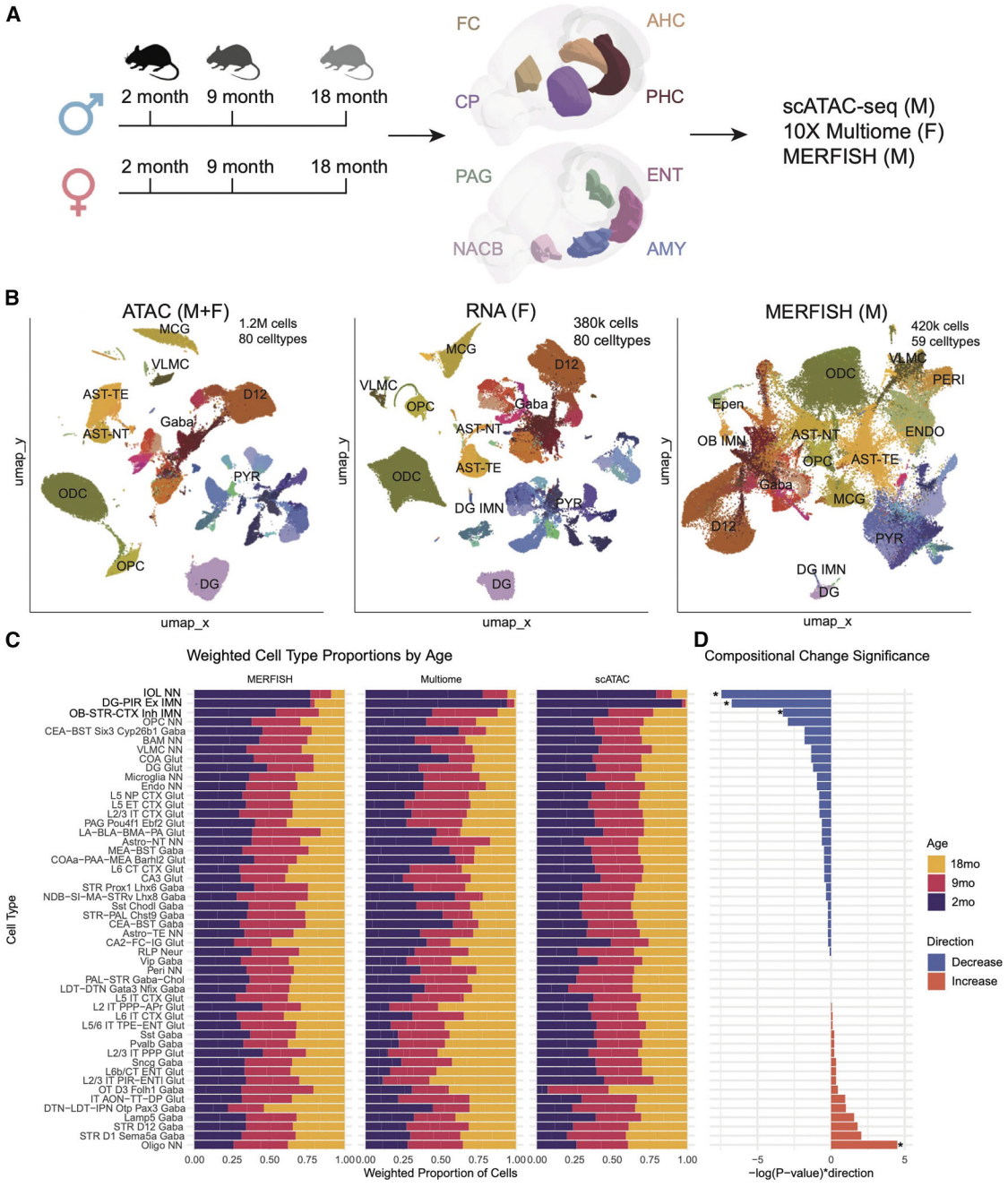

Figure 1. Single-nucleus multi-omic atlas of brain aging across eight regions in the mouse

(A) Schematic of experimental design showing brain regions profiled from male and female mice at 2, 9, and 18 months of age using snATAC-seq, 10× Multiome, and MERFISH.

(B) Uniform manifold approximation and projection (UMAP) of snATAC-seq (left), RNA-seq (center), and MERFISH (right) datasets, annotated by cell type.

(C) Weighted proportions calculated by normalizing cell counts by total cells per age group and modality, highlighting three progenitor populations that decline with age.

(D) Statistical significance of age-associated changes in cell-type proportions (Wilcoxon rank-sum test). Data are represented as the weighted proportion; the change in proportion is used for statistical comparison. *$p < 0.05$.

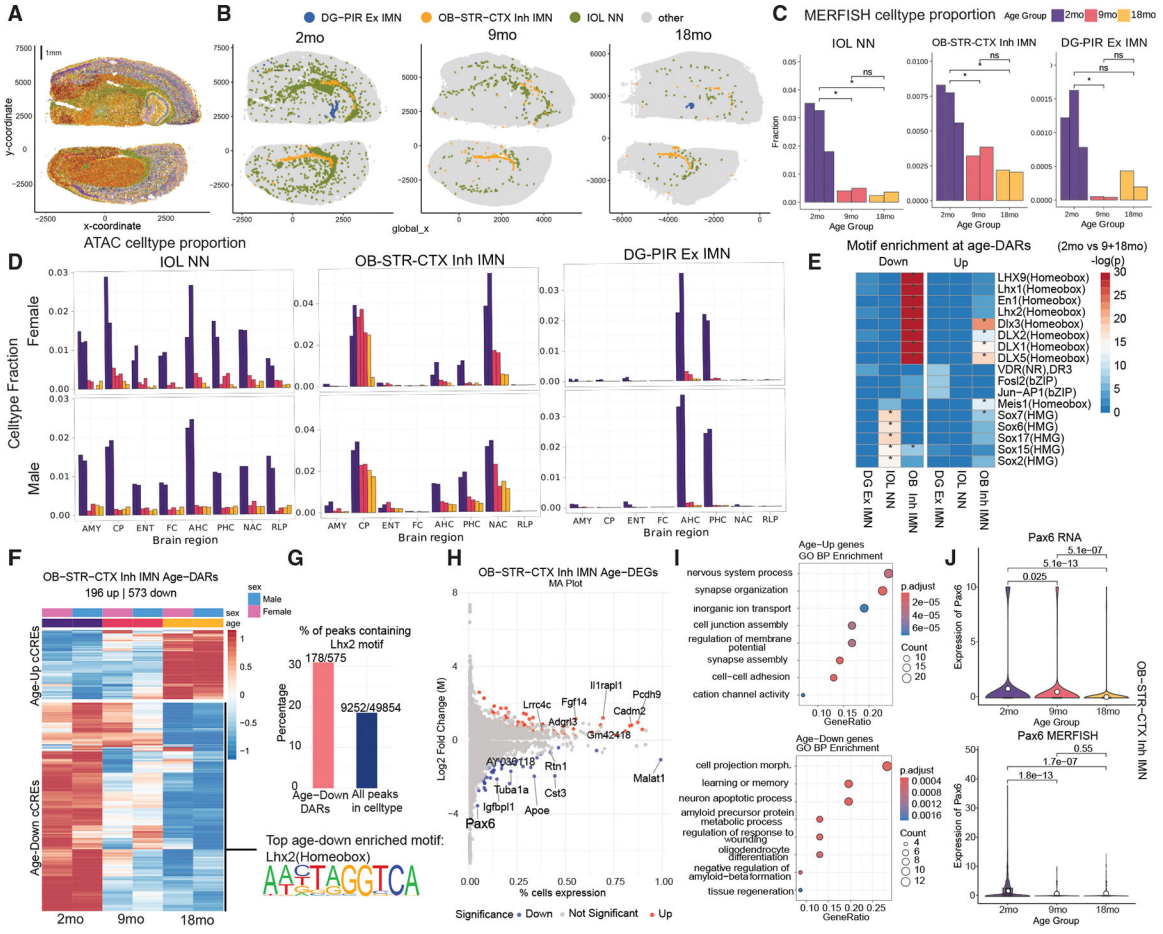

Figure 2. Aging depletes progenitor populations and disrupts neurogenic regulatory programs

(A) MERFISH spatial maps of brain slices (plates 46 and 69) with cells colored by annotated cell types (Table S1). The top left shows a scale bar representing 1 millimeter (mm).

(B) Representative MERFISH images across three ages showing immature oligodendrocytes (IOLs), OB-STR-CTX inhibitory immature neurons (Inh IMNs), and dentate gyrus (DG) progenitors.

(C) Age-associated changes in progenitor cell-type proportions from MERFISH data. Data are represented as the weighted proportion (normalized fraction of cells). Significance was determined by the Wilcoxon rank-sum test.

(D) Progenitor cell-type proportions from snATAC-seq across brain regions and sexes. Data are represented as the weighted proportion (the fraction of total cells in a sample labeled as that cell type).

(E) Motif enrichment analysis of age-associated differentially accessible cCREs in progenitor populations. Significance was determined by HOMER. The asterisk denotes significance (adj. $p < 0.01$).

(F) Heatmap showing normalized accessibility (Z score) of age-differential cCREs in OB-STR-CTX Inh IMNs, stratified by age and sex.

(G) Proportion of downregulated cCREs containing Lhx2 motifs in OB-STR-CTX Inh IMNs, shown in comparison to the proportion of all cCREs containing the Lhx2 motif.

Motif presence was identified using HOMER software. The bottom image shows the Lhx2 consensus motif.

(H) MA plot of age-differential gene expression (18 vs. 2 months) in OB-STR-CTX Inh IMNs. The *y* axis shows the $\log_2$ fold change, and the *x* axis shows the percentage of cells in which the gene is expressed. Significance for differential gene expression is defined as adj. $p < 0.05$ and absolute $\log_2 FC > 0.25$, determined by a likelihood ratio test (MAST).

(I) GO term enrichment for upregulated (top) and downregulated (bottom) genes in OB-STR-CTX Inh IMNs. Significance was determined by a hypergeometric test (clusterProfiler).

(J) Violin plot showing age-associated expression of Pax6, a direct target of Lhx2, in scRNA-seq (top) and MERFISH (bottom) datasets (expression at the single-cell level). Significance was determined by Wilcoxon rank-sum test.

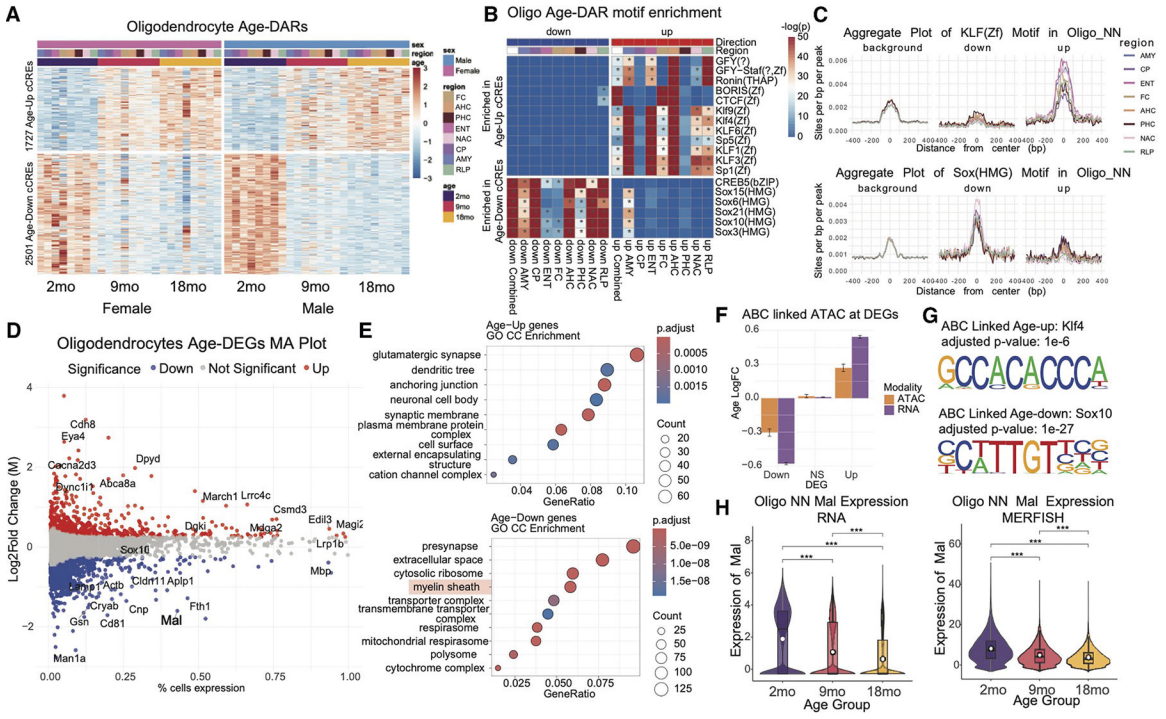

Figure 3. Aging oligodendrocytes exhibit transcriptional and chromatin changes associated with myelination loss and Sox factor decline

(A) Heatmap showing normalized accessibility (*Z* score) at age-differential cCREs in oligodendrocytes across brain regions and sexes.

(B) Motif enrichment of downregulated (left) and upregulated (right) age-differential cCREs in oligodendrocytes; asterisks denote significance (adj. $p < 0.01$) determined by HOMER.

(C) Aggregate motif accessibility plots for Klf1 and Sox6 in upregulated, downregulated, and non-changing peaks in oligodendrocytes (Oligo NNs).

(D) MA plot of age-differential gene expression (18 vs. 2 months) in oligodendrocytes. Significance for differential gene expression was determined by a likelihood ratio test (MAST).

(E) GO term enrichment analysis for upregulated (top) and downregulated (bottom) genes. Significance was determined by a hypergeometric test (clusterProfiler).

(F) Bar plot showing mean age $\log_2$ fold change ($\log_2$FC) of downregulated, non-significant, and upregulated genes, along with corresponding changes in linked cCREs from activity-by-contact (ABC) analysis, which predicts enhancer-promoter connections based on chromatin accessibility and 3D contact data from our companion paper (Zeng et al.[35]). Data are represented as the mean ($\log_2$FC) ± SEM.

(G) Motif logos for the most enriched motifs in peaks linked to upregulated (top) and downregulated (bottom) genes in aging oligodendrocytes. Significance was determined by HOMER using the hypergeometric distribution.

(H) Violin plot showing age-associated expression of the myelination gene Mal from scRNA-seq (left) and MERFISH (right) datasets (expression at the single-cell level). Significance for differential gene expression was determined by a likelihood ratio test (MAST).

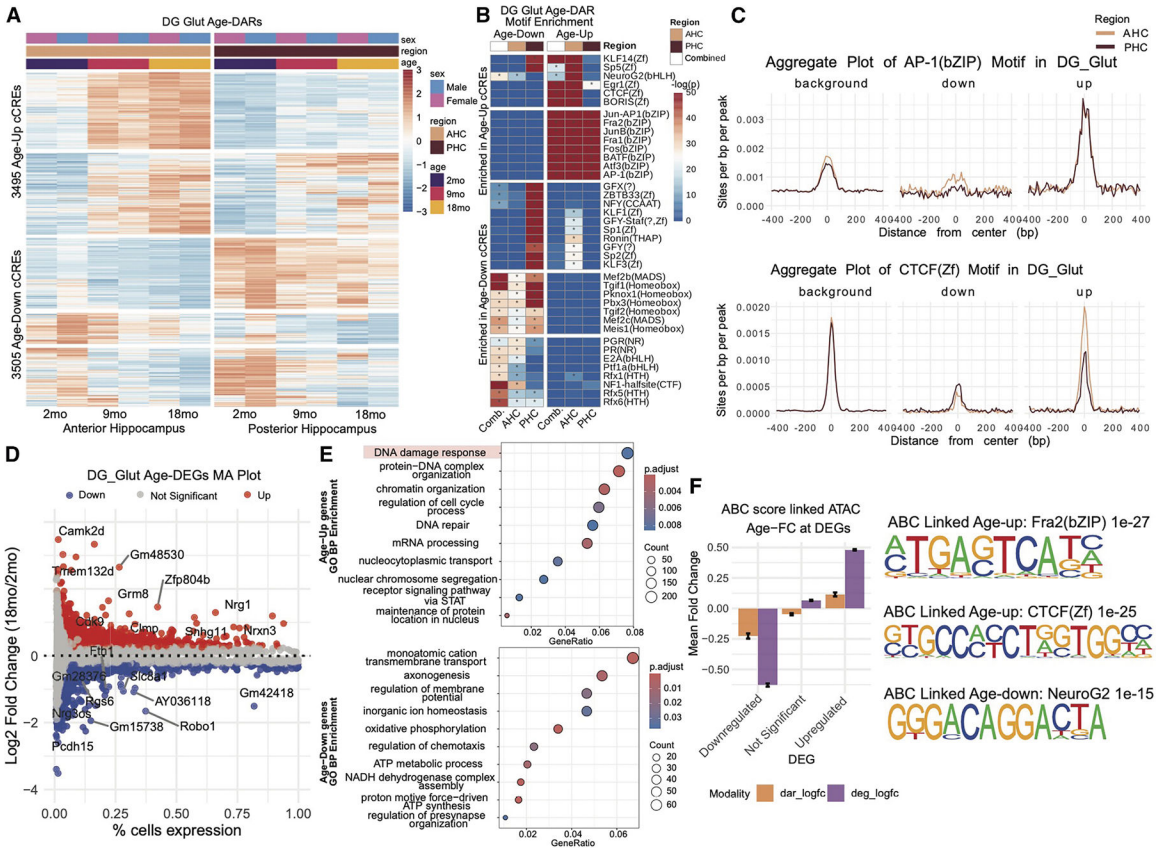

Figure 4. Aging induces region-specific regulatory reprogramming in dentate gyrus glutamatergic neurons

(A) Heatmap of normalized chromatin accessibility (*Z* score) at age-differential cCREs in dentate gyrus (DG) neurons across brain regions.

(B) Motif enrichment analysis of downregulated (left) and upregulated (right) age-differential cCREs using all peaks as background; asterisks denote significance (adj. $p <$ 0.01) determined by HOMER.

(C) Aggregate accessibility plots of AP-1 and CTCF motifs at upregulated, downregulated, and all cCREs across DG neuron regions produced by HOMER.(D) MA plot of age-differential gene expression between 2- and 18-month-old DG neurons. Significance for differential gene expression was determined by a likelihood ratio test (MAST).

(E) Gene Ontology (GO) enrichment analysis of genes upregulated with age. Significance was determined by a hypergeometric test (clusterProfiler).

(F) Bar plot showing mean age $\log_2$ fold change ($\log_2$FC) of downregulated, non-significant, and upregulated genes, along with corresponding changes in linked cCREs from activity-by-contact (ABC) analysis, which predicts enhancer-promoter connections based on chromatin accessibility and 3D contact data from our companion paper (Zeng et al.[35]). Data are represented as the mean ($\log_2$FC) ± SEM. Right: motif logos for the most enriched motifs in peaks linked to up- and downregulated genes.

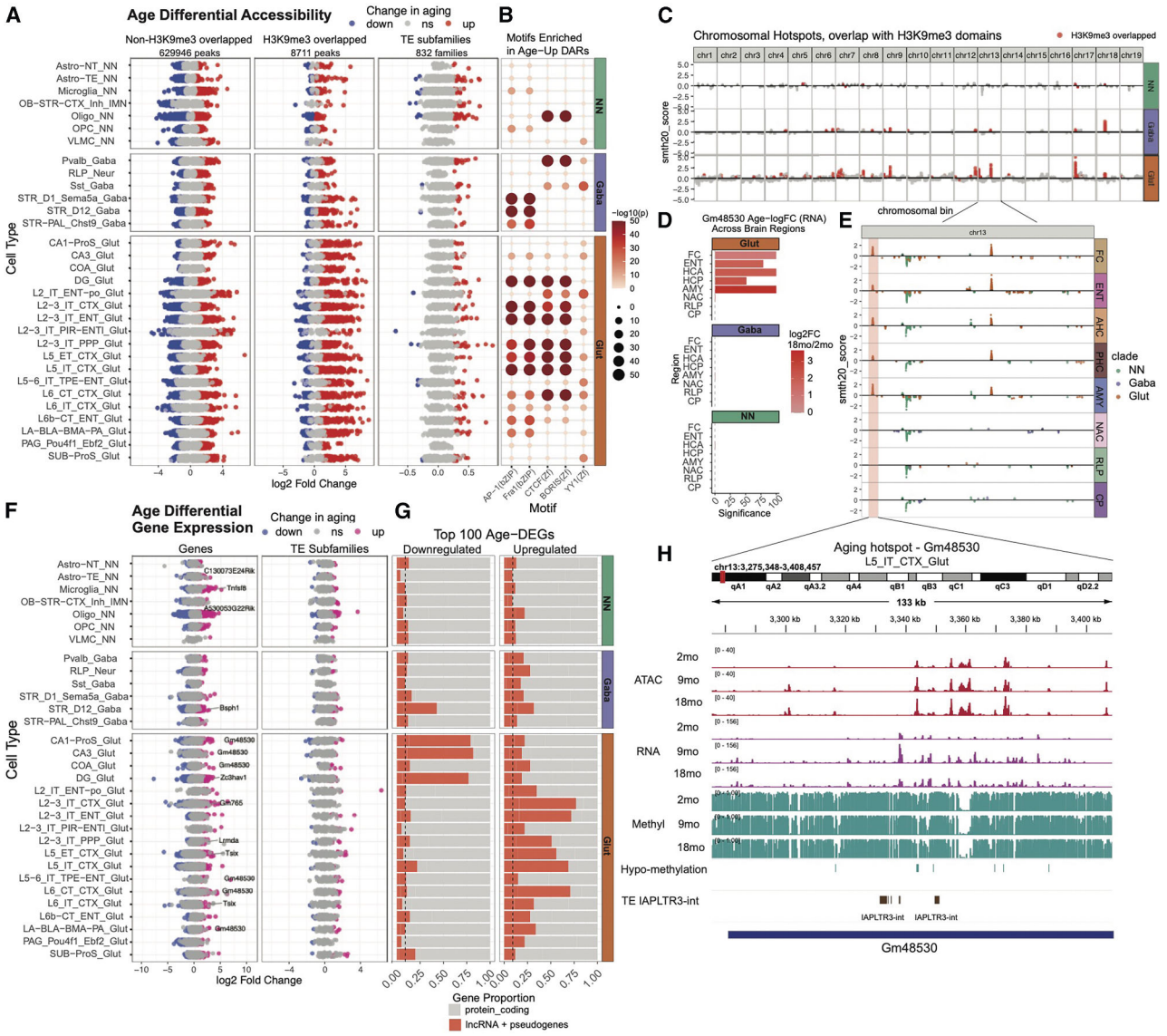

Figure 5. Upregulated accessibility and transcriptional shifts within heterochromatin-associated genomic hotspots

(A) Differentially accessible regions (DARs) in aging neurons. Left: non-H3K9me3 peaks show a balanced distribution of up- and downregulated peaks. Middle: H3K9me3-overlapping peaks are predominantly upregulated, especially in glutamatergic neurons. Right: transposable element (TE) subfamilies show widespread age-related increases in accessibility.

(B) Motif enrichment analysis of age-upregulated DARs across neuronal populations. Point size denotes the percentage of age-upregulated DARs containing motifs. Color indicates significance determined by HOMER using the hypergeometric distribution.

(C) Genomic hotspots with higher-than-expected density of DARs across cell types, colored by overlap with H3K9me3 domains. Hotspots were identified using Gaussian density scoring (see STAR Methods).

(D) Log_2 fold change and significance (−log10(adj. *p* value)) of lncRNA *Gm48530* expression across brain regions, located within an aging hotspot. Significance for expression change was determined by MAST (Model-based Analysis of Single-cell Transcriptomics; see STAR Methods).
(E) Chromosomal hotspot on chromosome 13 across brain regions; each point represents a cell type, colored by cell-type clade. Data are represented as the Gaussian smoothing hotspot score, where the distance from 0 indicates the magnitude of the score, with positive values representing chromatin regions gaining accessibility and negative values representing regions losing accessibility (see STAR Methods).
(F) Age-related transcriptional changes from scRNA-seq. Significance was determined with MAST (adj. $p < 0.05$). Left: log_2 fold change of genes across cell types, highlighting *Gm48530* among the most significantly upregulated. Right: log_2 fold change of TE subfamilies across cell types shows a broader trend of upregulation.
(G) Proportion of the top 100 most upregulated (right) and downregulated (left) genes that are long noncoding RNAs or pseudogenes. Data are represented as a proportion.
(H) Genome browser view of the chromosome 13 hotspot, including *Gm48530* and IAPLTR3-int, showing increased accessibility, expression, and hypomethylation with age. The *y* axis represents the reads per million (RPM)-normalized signal.

KEY RESOURCES TABLE

REAGENT or RESOURCE	SOURCE	IDENTIFIER
Chemicals, peptides, and recombinant proteins		
Tn5 transposase	QB3 Macrolab at UC Berkeley	N/A
SPRISelect reagent	Beckman Coulter	Cat# B23319
DRAQ7	Cell Signaling	Cat# 7406
NEBNext High-Fidelity PCR Master Mix	NEB	Cat# M0541L
LightCycler 480 SYBR Green I Master Mix	Roche	Cat# 04707516001
DTT nuclei permeabilization buffer	Sigma-Aldrich	Cat# 646563-10X
IGEPAL-CA630	Sigma-Aldrich	Cat#I8896
1X cOmplete EDTA-free protease inhibitor cocktail tablets	Roche Diagnostics	11873580001
Critical commercial assays		
gentleMACS Octo Dissociator	Miltenyi	Cat# 103-095-937
Chromium Controller	10× Genomics	Instrument
Chromium Next GEM Single-Cell Multiome ATAC + Gene Expression Reagent Bundle	10× Genomics	Cat# 1000283
Chromium Next GEM Chip J	10× Genomics	Cat# 1000234
NovaSeq 6000	Illumina	Instrument
S4 Flow Cell	Illumina	20028312
NextSeq 500	Illumina	Instrument
MERSCOPE 500 Gene Imaging kit	Vizgen	Cat# 10400006
Vizgen sample preparation kit	Vizgen	Cat# 10400012
Deposited data		
Raw sequencing data (snATAC, snRNA)	This paper; Li et al.[18]	SRA: PRJNA1248586
Processed data (snATAC, snRNA)	This paper; Li et al.[18]	GEO: GSE294772
Female single-cell Contact	Zeng et al.[35]	GEO: GSE292803
Male Cell type pseudo-bulk AllC	Zeng et al.[35]	GEO: GSE313770
Female Cell type pseudo-bulk AllC	Zeng et al.[35]	GEO: GSE292803
Experimental models: Organisms/strains		
Mouse: C57BL/6J	The Jackson Laboratory	JAX: 00064
Oligonucleotides		
Custom Tagmentation Oligos	This paper	NA
Custom PCR Primers	This paper	NA
Custom Sequencing Primers	This paper	NA
Dual Index Kit	10x Genomics	Cat# 1000215
Software and algorithms		

REAGENT or RESOURCE	SOURCE	IDENTIFIER
SnapATAC2 (v2.5.1)	Zhang et al.[19]	https://github.com/scverse/SnapATAC2
Seurat (v5.0.0)	Satija Lab	https://satijalab.org/seurat/
Harmony (v1.2.3)	Korsunsky et al.[20]	https://github.com/immunogenomics/harmony
MACS3 (v3.0.0)	Zhang et al.[22]	https://github.com/macs3-project/MACS
MAST (v1.28.0)	Finak et al.[25]	https://github.com/RGLab/MAST
CellPose (v2.1.1)	Stringer et al.[58]	https://github.com/MouseLand/cellpose
Scanpy (v1.10.0)	Wolf et al.[59]	https://github.com/scverse/scanpy
HOMER (v4.11)	Heinz et al.[60]	http://homer.ucsd.edu/homer/
Analysis code	This paper	https://github.com/luisajamaral/aging_mouse_brain_code